A Quasi-static Hyper-resistive Model of Ultra-high-energy Cosmic-ray Acceleration by Magnetically Collimated Jets Created by Active Galactic Nuclei

T. Kenneth Fowler[1], Hui Li[2] , and Richard Anantua[1,3]
[1] University of California, Berkeley, CA 94720, USA
[2] Los Alamos National Laboratory, Los Alamos, NM 87545, USA; hli@lanl.gov
[3] Harvard-Smithsonian Center for Astrophysics, Cambridge, MA 02138, USA
Received 2019 March 15; revised 2019 August 28; accepted 2019 September 14; published 2019 October 24

Abstract

This is the fourth in a series of companion papers showing that when an efficient dynamo can be maintained by accretion disks around supermassive black holes in active galactic nuclei, it will lead to the formation of a powerful, magnetically collimated helix that could explain the observed jet/radiolobe structures on very large scales. Here, we present a hyper-resistive kinetic theory that shows how different instabilities can cause the slowly evolving magnetically collimated jets to accelerate ions and electrons in different regions of jets and lobes. In particular, we propose that the Drift Cyclotron Loss Cone instability at the ends of jets can accelerate ions up to the observed ultra-high-energy cosmic rays with energies $\approx 10^{20}$ eV. Based on this jet/lobe structure model and its associated acceleration processes, we estimate cosmic-ray intensities and likely radiative signatures and compare them with observations.

Key words: acceleration of particles – accretion, accretion disks – cosmic rays – galaxies: jets

1. Introduction

Relativistic magnetized jets, powered by supermassive black holes (SMBHs), are observed to propagate on scales from au to Mpc and emit radiation from meter wavelengths to TeV γ-rays. High-resolution radio/optical imaging and multi-wavelength/ messenger campaigns are elucidating the conditions under which this happens. Understanding astrophysical jets spanning huge spatial and temporal scales, often with extreme physical conditions, remains one of the most challenging problems in astrophysics.

Active galactic nucleus (AGN) jets can be characterized by four broadly defined spatial scales: (1) the "engine" near the black hole, with Schwarzschild scale $R_s = 2GM/c^2$; (2) the putative "flare" region where multi-wavelength and multi-messenger emissions exhibit strong variabilities, with scale $R_f = 2GM/v^2$ for $v = \sigma_*$ (where σ_* is stellar velocity dispersion) or sound speed $v = c_S$ (then R_f is approximately the Bondi radius); (3) the "propagation" region where jets move through the host galaxy's ISM and beyond; and (4) the "termination" region extending to Mpc. As noted in the Abstract, here we only consider circumstances in which an efficient electric dynamo can be created in the engine region, strong enough to create jets punching through the flare region. Then spatial scales come to be fixed by magnetic pressure rather than gravitational attraction, possible because the collimated magnetic jets have field pressures $B^2/(8\pi) \gg 1/2 n_{\rm amb} m_i c_S^2$ in the ambient medium far from the black hole.

In the regime under consideration, dissipation by ion collisions and electrical resistance is often negligible, leaving dissipation by radiation. As described in several recent excellent reviews (Madejski & Sikora 2016; Blandford et al. 2019), AGN jets are strong emitters of electromagnetic radiation, implying very efficient particle acceleration, often in situ in the jet and lobe regions. The most promising mechanisms for producing relativistic AGN jets are MHD acceleration from an accretion disk around a black hole, in both hydromagnetic limit (e.g., Blandford & Payne 1982; Ustyugova et al. 1999; Narayan et al. 2007, among many others) and the Poynting flux limit (e.g., Blandford 1976; Lovelace 1976; Lynden-Bell 1996; Li et al. 2001; Lovelace et al. 2002; Komissarov et al. 2007, among many others). In addition, major progress has been made using general relativistic MHD (GRMHD) codes to study the extraction of rotational energy from a spinning black hole (e.g., Blandford & Znajek 1977; Hawley & Krolik 2006; McKinney et al. 2012, among many others).

On large scales, jet morphologies (such as lobes, hot spots, and filaments) and their associated instabilities have also been investigated extensively. In particular, the pioneering work by Norman et al. (1982) sets the stage for three decades of jet studies. Although magnetic fields have been actively included in some of these studies, the overall behavior has been predominantly determined in the hydrodynamic limit (e.g., Heinz 2014, among many others). The relative importance of kinetic energy and magnetic energy in jets and radiolobes, however, remains a subject for extensive studies and debates.

In recent years, however, there is an important shift in our view of magnetic fields in jets over all scales, from near the SMBH, to parsec-scale jets, to kpc–Mpc jets and lobes (e.g., X-ray cavities; Diehl et al. 2008). In particular, one line of research is the so-called magnetic tower model (MTM; e.g., Lynden-Bell 1996, 2003; Li et al. 2001, 2006; Nakamura et al. 2006, 2007; Guan et al. 2014; Gan et al. 2017). Perhaps the most important feature of MTM is the presence of a global current structure where an outgoing current flows out of the black hole accretion region, along the central spine of the jet to the edges of lobes, then returns along a boundary that separates the magnetized region from the unmagnetized surrounding plasmas. (In practice, this boundary can be identified as the layer where the radio emission of lobes sharply drops below the detection limits.) MTM differs from the more traditional hydrodynamic jets in that it always maintains a global current structure, even though on global scales magnetic energy and
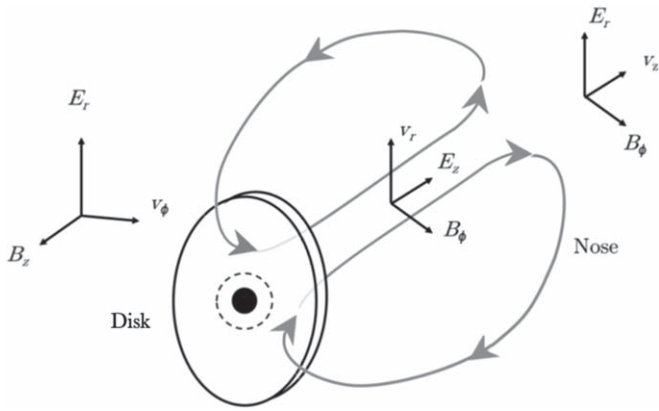
Figure 1. Sketch of an accretion disk accelerator producing an axisymmetric jet current j_z of slowly growing length L, showing the poloidal component of two of the closed current loops driven by an electrostatic field E_r due to disk rotation. The E_r in the disk extracts energy from accretion. The E_z in the jet provides an initial acceleration of electrons and ions. The E_r in the nose contains the main cosmic-ray accelerator.

plasma energy, when summing over the volume, can become comparable.

Another essential challenge in jet models is the conversion of electromagnetic energy to plasma energy. At macro-scale, many studies have examined the gradual jet acceleration by magnetic forces as well as dissipation of magnetic fields. In addition, magnetic fields can dissipate if there exists global MHD instability, with kink instability being the most plausible candidate (e.g., Spruit et al. 1997; Begelman 1998; Nakamura et al. 2007; Mizuno et al. 2014; Singh et al. 2016, among many others). At both macro and microscopic levels, in addition to shock acceleration, particle acceleration by relativistic reconnection has gained increasing attention because of its direct relevance in the magnetically dominated regimes (e.g., Lazarian & Vishniac 1999; de Gouveia Dal Pino & Lazarian 2005; Kowal et al. 2011; Liu et al. 2011; Guo et al. 2014; Sironi & Spitkovsky 2014; Werner et al. 2016, among many others). AGN jets and lobes have also long been thought as possible candidates for extra-galactic cosmic rays, including the ultra-high-energy cosmic rays (UHECRs), with energies up to $\approx 10^{20}$ eV (e.g., Cronin 1999). Many explanations have been offered (e.g., Bierman 1997), none yet fully satisfactory (Blandford et al. 2019).

This paper is the fourth in a series of papers exploring a quasi-static model of UHE cosmic-ray production in jets created by accretion around SMBHs inside AGNs. The purpose of this paper is to show how our jet model developed in earlier papers can become a quasi-static accelerator producing UHE cosmic rays with properties in general agreement with cosmic-ray observations (Pierre Auger Collaboration 2007, 2014, 2017).

As suggested in Colgate & Li (2004), we have taken laboratory spheromaks as the likely paradigm for the observed quasi-stable behavior of AGN jets enduring for times of order 10^8 yr (Colgate & Li 2004; Beskin 2010). Spheromaks consist of a magnetized gun injecting plasma into an evacuated vessel (Hooper et al. 2012; Zhai et al. 2014). Initially the plasma is a magnetically collimated jet surrounded by a largely empty lobe bounded by its return current. A sketch is shown in Figure 1, based on the SSPX spheromak (Figure 2 of Colgate et al. 2015; Hooper et al. 2012). The return current is confined radially by the vessel wall (or ambient pressure in AGN jets). Different from the laboratory spheromaks in which turbulent diffusion of

current out of the central column would begin to fill the lobe when the jet encounters the laboratory vessel end wall, the AGN jets are free to propagate into the background medium. Their lobes are largely empty due to weak diffusion compared with the forward motion of the jet. This was observed to give a nearly vacuum field $B_\phi \propto 1/r$ in the lobe based on simulations in Nakamura et al. (2006), consistent also with the weak effects of kink modes during jet formation in SSPX (see Figure 2 Colgate et al. 2015).

Although our jet and lobe model is inherently 3D, many key features can be obtained in 2D axisymmetric terms. We will describe the jet by its mean field obtained by averaging over the azimuthal angle ϕ and fluctuation timescales. This mean field satisfies $\boldsymbol{j} \times \boldsymbol{B} = 0$, describing a self-confined "screw pinch" with magnetic field $\boldsymbol{B}$ and $\boldsymbol{j} = (c/4\pi)\nabla \times \boldsymbol{B}$. Most of the current $\boldsymbol{j}$ is concentrated in a column centered on the axis of symmetry, giving a magnetic field $B_\phi \propto 1/r$ inside the large ("radiolobe") volume encompassed by the return current. Accumulating magnetic energy (inductance $\ln R/a$) slows down the jet to a speed given by (Colgate et al. 2015)

$$dL/dt \approx fc/\ln(R/a) \approx 0.01c, \tag{1}$$

where typically the radiolobe radius $R \approx 10^{23}$ cm and the jet radius $a \approx 3 \times 10^{14}$ cm, with some dissipation in shocks and particle acceleration given by $f \approx 1/4$ (Colgate et al. 2015).

Thus we arrive at a slowly evolving magnetic structure that can only accelerate particles parallel to $\boldsymbol{B}$. Figure 1 illustrates the fields producing particle acceleration in different regions. It does this first by an electrostatic sheath at the disk corona that serves to launch ions against gravity (Lovelace 1976; Appendix A, Colgate et al. 2015). Then inside the jet an accelerating electric field is generated by the twisting and bending of the jet current column (MHD kink modes). Expanding $\boldsymbol{j}$ in Fourier modes in azimuthal angle ϕ and averaging over ϕ gives only the axisymmetric configuration in Figure 1. And simulations show that most of the power is concentrated in this axi-symmetrized jet, constituting a two-dimensional (2D) "mean-field" description of the jet (Carey 2009; Carey et al. 2011).

The growth of energy in MHD kink modes (both ideal modes and tearing modes producing magnetic reconnection) implies that an axi-symmetrized electric field must exist with a sign to extract energy from the mean-field current. Ion acceleration without reconnection has been observed in experiments (Rusbridge et al. 1997), and the accelerating field was observed in ideal MHD simulations discussed in Colgate et al. (2015). Acceleration of electrons by this 2D mean field could account for all electromagnetic radiation, while acceleration of ions by this field is the first stage of our cosmic-ray accelerator. That two stages of acceleration are required follows from radiative losses by ions following the twisted field lines of the jet. This will turn out to limit ion energies to $\approx 3 \times 10^{16}$ eV. That a further stage of acceleration will occur in the jet nose, all the way to the 10^{20} eV produced by the dynamo, is the main message of this paper.

Again learning from modeling spheromak experiments, we will formulate particle acceleration as hyper-resistivity $\mathcal{D}$ in a mean-field Ohm's law, giving

$$\boldsymbol{E} + c^{-1}\boldsymbol{v} \times \boldsymbol{B} = \mathcal{D}. \tag{2}$$

Inside the accretion disk, $\mathcal{D}$ represents the magneto-rotational instability (MRI) shown to create a dynamo in Balbus & Hawley (1998). Inside the collimated jet, $\mathcal{D}$ represents MHD

kink modes and also "two-stream" interaction of counter-streaming ions and electrons. At the nose, $\mathcal{D}$ will represent ion cyclotron resonance with drift waves that constitutes the final stage of UHE cosmic-ray acceleration (Fowler et al. 2009a; Fowler & Li 2016). Since turbulence is involved, our predictions using $\mathcal{D}$ are necessarily order-of-magnitude estimates, useful mainly as a guide to important phenomena missing in other work, and as guidance for observations that might support the model and for simulations including both MHD and kinetic processes.

We recognize that magnetic collimation over enormous distances is controversial. Furthermore, as shown by GRMHD simulations, initially accretion disks do not launch magnetically collimated jets because the radial electric fields tend to de-collimate the jets. A new result in Appendix A attempts to reconcile our collimated jets with the GRMHD results. Otherwise we rely on self-consistency as justification for the model, first concerning disks as boundary conditions for jet launching in Colgate et al. (2014) and second concerning the integrity of collimated jets undergoing kink instability in Colgate et al. (2015). We find that jets are launched electrostatically, with too little mass to sustain significant relativistic mass flows in jets, and negligible centrifugal ejection of mass from the accretion disk (Blandford & Znajek 1977; Blandford & Payne 1982). Alternative explanations of superluminal effects and other evidences for relativistic flows are suggested in Section 2 of Colgate et al. (2015). That paper also reviews observational evidence for magnetic collimation (with new data in Giovannini et al. 2018); evidence of radiolobes as largely empty voids with magnetic field $\propto 1/r$ (Owen et al. 1989; McNamara & Nulsen 2007; Diehl et al. 2008; Kronberg et al. 2011); and laboratory evidence for collimated jet propagation under sub-Alfvénic propagation conditions similar to our AGN jet model (Hooper et al. 2012).

The main alternatives to our cosmic-ray acceleration model involve transient shocks and/or magnetic reconnection (Singh et al. 2016; Blandford et al. 2019; de Gouveia Dal Pino et al. 2019; and references therein). In Section 6, we note that these models could also be represented by hyper-resistivity $\mathcal{D}$ in Equation (2). Alternative interpretations of $\mathcal{D}$ would not alter our conclusion in Section 3.2 that no more than 1% of the dynamo power is deposited along the jet. This leaves the nose as the main site for cosmic-ray acceleration at the higher power levels we find necessary to account for UHE cosmic-ray intensity on Earth. The collimated jet serves mainly as a conduit of power between the accretion disk and the nose. As noted in Colgate et al. (2014, 2015), collimation allows deviations from a straight path for jets deflected by the ambient, as is sometimes observed (Begelman et al. 1984). Analogous WKB solutions could describe such jets. The minimum length required for sustained collimation (straight or curved) will turn out to be of order ≈ 10 kpc, sufficient to accelerate ions to the maximum energy allowed by curvature radiation in the collimated jet.

The remainder of the paper is organized as follows. Section 2 summarizes jet parameters needed in later sections, tabulated in Table 1. Section 3 discusses ion acceleration. Section 4 derives the cosmic-ray energy distribution and compares this with the UHE cosmic-ray intensity at the Pierre Auger Observatory. Section 5 discusses electromagnetic radiation as a signature of

Table 1
Jet Parameters (M_8 = Black Hole Mass M in Units of 10^8 Solar Masses)

Jet radius $(a\Omega_a/c) = (f/b)^{1/2} \approx 0.22$	$a = 3 \times 10^{14} M_8$ cm
Jet length $L = 0.01c\tau$, $\tau = 10^8$ yrs	10^{24} cm
Average radiolobe radius $R = 0.1L$	10^{23} cm
Magnetic field B_a	$1500 M_8^{-1/2}$ Gauss
Dynamo current $I = aB_a c/2$	$0.7 \times 10^{28} M_8^{1/2}$ esu s^{-1}
Dynamo voltage $\mathcal{V} = b(a\Omega_a/c)aB_a = aB_a$	$1.4 \times 10^{20} M_8^{1/2}$ volts
Jet power $I\mathcal{V}$	$3.3 \times 10^{45} M_8$ erg s^{-1}
Jet density $n_I = (I/ec\pi a^2)$	$1.4 \times 10^{-3} M_8^{-3/2}$ cm^{-3}

Table 2
Model Predictions

Jet Properties	
Jet length $L = 10^{24}$ cm = 300 kpc	Table 1
Radiolobe radius $R \approx 0.1L$	Table 1
Synchrotron Radiation	
Synchrotron luminosity	Equation (35)
Synchrotron wavelength $\lambda_{\mathrm{SYN}} = 7(\gamma_{\mathrm{Le}}/n)$ cm	Equation 36(b)
Synchrotron opening angle $\Theta \approx 0.01$ radians	Equation (37)
Maximum Electron Energy $17 M_8^{5/8}$ TeV	Equation 11(b)
UHR Cosmic Rays	
Maximum UHECR energy $1.4 \times 10^{20} M_8^{1/2}$ eV	Equation 18(b)
UHECR intensity on Earth	Equations (30)
UHECR energy spectrum $I_{\mathrm{CR}}(E) \propto E^{-p} (p \approx 3)$	Equation 25(b)

the model. Section 6 discusses transient versus quasi-static acceleration. Section 7 summarizes results, with predictions listed in Table 2. Appendix A attempts to resolve differences between our model and GRMHD simulations, and Appendix B includes useful plasma formulas.

We use cylindrical coordinates $\{r, \phi, z\}$ in which the disk spins about a fixed z-axis with angular frequency $\mathbf{\Omega}$ pointing along the $+z$-direction in the inner region of the disk, giving positive toroidal magnetic field B_ϕ and negative B_z in the same region. Except as noted, units are cgs, often introducing c, the speed of light.

2. Jet Parameters

The key quantities needed in the remainder of the paper concern the final jet velocity dL/dt and numbers associated with the collimated jet (Central Column) where most of the gravitational power is deposited. As in Colgate et al. (2014, 2015), the jet column radius a is defined as the inner radius of a Diffuse Pinch characterized by Keplerian rotation in the disk, while the Central Column at $r < a$ is described by an electric circuit with current I and voltage $\mathcal{V}$ (McDonald & Thorne 1982; Lovelace & Kronberg 2013).

Prescriptions for calculating jet parameters are given in Colgate et al. (2015), in terms of the magnetic field $B_\phi = B_z \equiv B_a$ and rotation Ω_a at $r = a$, and an accretion rate $dM/dt = 2 \times 10^{25} M_8$ gm s^{-1} for black hole mass M in units of 10^8 solar masses, where $dM/dt = M/\tau$ with jet lifetime $\tau = 10^8$ yr (Colgate & Li 2004; Beskin 2010). Simultaneous solution of disk angular momentum $1/2(dM/dt)\Omega_a = aB_a^2$ and jet power $I\mathcal{V} = fc^2(dM/dt)/4$ gives the parameters in Table 1. Here $f = 1/4$ is the estimated efficiency of converting gravitational power into jet power and $b = [1 + \int_{R_s}^{a} dr(E_r(r)/aE_r(a))] = 5$ is a fitting factor discussed in Appendix B of Colgate et al. (2015). Otherwise, numbers

accurately represent the rectangular Grad–Shafranov jet solution shown in Figure 1 of Colgate et al. (2015) with boundary conditions at the disk derived in Colgate et al. (2014). The Keplerian Diffuse Pinch region at $r \geqslant a$ contains 40% of the current but only 15% of the jet power. Estimates of the efficiency f effectively absorb any effects of viscosity, found to be negligible in our ordering scheme in Appendix A of Colgate et al. (2014). As discussed in Appendix A of Colgate et al. (2015), the low jet density listed in Table 1 implies a relativistic Alfvén velocity equal to c.

3. ION Acceleration in AGN Jets

We now begin our discussion of how magnetic energy is converted to UHE cosmic rays, using known physics of plasma turbulence discussed in Appendix B. For simplicity, we assume ions to be protons, known to be constituents of most UHECRs (Cronin 1999, albeit uncertainties in composition remain), though the model applies to any ion species. We assume that jet composition is electron–proton plasma. The model also describes electron acceleration yielding synchrotron radiation, discussed in Section 5. We neglect positrons that do not contribute much to the current, due to two-stream interaction with electrons, similar to ion–electron two-stream interaction discussed as follows.

We begin with two points distinguishing our model of UHE cosmic rays. First, while AGN jets are mainly observed by synchrotron radiation, the synchrotron power is known to be a negligible fraction of overall AGN power and electrons play a secondary role in our model of ion acceleration. Second, as discussed in the Introduction, our cosmic-ray accelerator model is a two-stage ion accelerator. The first stage occurs in the Central Column, limited by ion radiation to energies well below UHECRs. The second stage occurs in the nose-end of the jet. In both stages, acceleration is due to plasma turbulence (hyper-resistivity in Ohm's law). What distinguishes these two regions is the size of the ion Larmor radius r_{Li}. In the Central Column, $r_{\mathrm{Li}} \ll a$ giving MHD current-driven kink modes as the main source of hyper-resistivity. In the nose with magnetic flux width Δ, the fall of $B_\phi \propto 1/r$ finally yields $r_{\mathrm{Li}} \approx \Delta$, whereupon ions resonating with electron drift waves are known to produce a powerful turbulence, specifically the Drift Cyclotron Loss Cone (DCLC) instability explained in Section 3.3.2 that could both accelerate ions to 10^{20} eV energies and eject enough ions as cosmic rays to account for the UHECR intensity on Earth (see Section 4).

The electrons behave passively in the DCLC turbulence so they are not accelerated in the nose, while ions resonant with the electron waves in the nose are strongly accelerated. For a different reason, electrons play a passive role in kink instability in the Central Column. Again this is due to kinetic effects not included in MHD—namely, the two-stream instability between counter-flowing ions and electrons accelerated by the kink-mode turbulence. Because of their difference in rest mass, two-stream instability scatters electrons sufficiently to eliminate the electron current in our reference frame, while ions are not much affected. Thus the kink-mode accelerator in the Central Column produces current as a mono-energetic ion beam with sufficient energy to produce DCLC instability in the nose.

The mathematics supporting this picture is developed as follows. A key feature is the role of turbulence-driven hyper-resistivity in Ohm's law. Like earlier cosmic-ray models, hyper-resistivity depends on correlations in turbulent fluctuations to

give additive additions to particle energy. Self-correlated hyper-resistive ion acceleration by kink modes was observed in the SPHEX spheromak experiment, discussed as follows. Two-stream instability is discussed in Appendix B.2.

3.1. Acceleration by Turbulence

Our accelerator model begins with the relativistic acceleration equation, with acceleration of momentum $\boldsymbol{p}$ of a particle given by

$$\frac{d\boldsymbol{p}}{dt} = e\left(\boldsymbol{E} + \frac{1}{c}\frac{\boldsymbol{p}}{m\gamma_{\mathrm{L}}} \times \boldsymbol{B} - \boldsymbol{E}_{\mathrm{rad}}\right), \tag{3}$$

where $\boldsymbol{E}_{\mathrm{rad}}$ represents radiation loss. While taking $\boldsymbol{p} \cdot \frac{d\boldsymbol{p}}{dt} = e\boldsymbol{p} \cdot (\boldsymbol{E} - \boldsymbol{E}_{\mathrm{rad}})$ confirms that only $\boldsymbol{E}$ can accelerate ions parallel to $\boldsymbol{B}$ in our reference frame fixed in the disk, by now a number of magnetic acceleration mechanisms have been identified in which $\boldsymbol{B}$ invokes $\boldsymbol{E}$ in moving structures (shocks, clouds, etc.). Acceleration by turbulence can be thought of this way, whereby accelerated particles encounter self-organized fluctuations in a plasma.

Formally, in our model energy conversion comes from $\int d\boldsymbol{x}\,\langle \boldsymbol{j} \cdot \boldsymbol{E}\rangle \equiv f_{\mathrm{conv}} I\mathcal{V}$, where the integral is over the entire structure of the magnetic jet and $\langle...\rangle$ represents an average over the toroidal angle ϕ and an average over fluctuations. The integral is dominated by the Central Column, which carries most of the power to the nose in Figure 1. The average $\langle...\rangle$ yields a turbulence-generated $\langle \boldsymbol{E}\rangle$ that could serve as a quasi-steady accelerator. Most of the kinetic power is contained in $\langle \boldsymbol{j}\rangle \cdot \langle \boldsymbol{E}\rangle$, accounting for the observation of quasi-steady acceleration of ions in the SPHEX spheromak mentioned previously. In this section we will focus on the quasi-steady acceleration of ions and defer electron acceleration to Section 5. To calculate ion acceleration, we determine $\boldsymbol{E}$ from the relativistic form of Ohm's law:

$$\boldsymbol{E} - \sum\left[\int d\boldsymbol{p}\left(\frac{f}{n}\right)\left(\frac{m_e \gamma_{\mathrm{Le}}}{m\gamma_{\mathrm{L}}}\right)\frac{1}{c^2}\boldsymbol{u}(\boldsymbol{u} \cdot \boldsymbol{E})\right]$$
$$+ \frac{1}{c}\boldsymbol{v} \times \boldsymbol{B} - \left(\frac{\boldsymbol{j}}{nec}\right) \times \boldsymbol{B} - \mathcal{D} = \boldsymbol{0}. \tag{4}$$

Here Σ sums over ions and electrons, $\boldsymbol{u} = (\boldsymbol{p}/m\gamma_{\mathrm{L}})$, and $\boldsymbol{u}(\boldsymbol{u} \cdot \boldsymbol{E})$ arises from $\partial\gamma_\perp/\partial p$ in an integration by parts (Montgomery & Tidman 1964). The Hall term $\left(\frac{\boldsymbol{j}}{nec}\right) \times \boldsymbol{B}$ applies only to $\boldsymbol{E}_\perp$ giving MHD. From the radiation discussion that follows, we will learn that always the ion Lorentz factor $\gamma_{\mathrm{Li}} \geqslant \gamma_{\mathrm{Le}}$, which allows us to order all ion terms in Ohm's law as the ratio of electron rest mass to ion rest mass, hence negligible. Dropping the Hall term, we obtain for relativistic electrons

$$\boldsymbol{E}_\perp + \frac{1}{c}\boldsymbol{v} \times \boldsymbol{B} = \mathcal{D}_\perp, \tag{5a}$$

$$C_{\mathrm{Rel}}\boldsymbol{E}_\parallel \equiv \boldsymbol{E}_\parallel - \sum\left[\int d\boldsymbol{p},\right.$$
$$\left.\times \left(\frac{f}{n}\right)\left(\frac{m_e \gamma_{\mathrm{Le}}}{m\gamma_{\mathrm{L}}}\right)\frac{1}{c^2}\boldsymbol{u}_\parallel(\boldsymbol{u} \cdot \boldsymbol{E})\right] = \mathcal{D}_\parallel, \tag{5b}$$

$$C_{\text{Rel}} \approx 1 - \sum \int d\boldsymbol{p} f_{0e} (1/c^2)$$
$$\times [u_\parallel^2 + u_\parallel(\boldsymbol{u}_\perp \cdot \boldsymbol{E}/E_\parallel)] \approx \int d\boldsymbol{p} f_{0e} (u_\perp^2/c^2) \approx 1, \tag{5c}$$

$$\mathcal{D} = -\frac{1}{c}\langle \boldsymbol{v}_1 \times \boldsymbol{B}_1 \rangle, \tag{5d}$$

where, in Equation 5(c), we first use $\int d\boldsymbol{p} f_{0e} u_\parallel = 0$ by two-stream instability to eliminate the term linear in $u_\parallel$, then substitute $u_\parallel^2/c^2 = 1 - (u_\perp^2/c^2)$ to obtain the final result on the right-hand side. Here, we write out $\mathcal{D}$ explicitly giving hyper-resistivity for MHD fluctuations. The bracket $\langle...\rangle$ indicates an axisymmetric smooth average over fluctuations. Equation 5(a) yields MHD jet propagation, while $C_{\text{Rel}}\boldsymbol{E}_\parallel = \mathcal{D}_\parallel$ is the relativistic accelerator in the Central Column of the jet. Note the crucial role of two-stream instability in defeating a relativistic cancellation of the accelerator parallel to $\boldsymbol{B}$ in our reference frame.

3.2. Ion Acceleration in the Central Column

We make the assumption, justified later, that ions and electrons in the Central Column can be described by orbits consisting of circles with small Larmor radii $\ll a$, gyrating around a "guiding center" momentum $p_\parallel$ mainly directed along magnetic field lines. Using Ohm's law, the acceleration equation, Equation (3), becomes

$$\frac{dp_\parallel}{dt} = e(E_\parallel - E_{\text{RAD}}), \tag{6a}$$

$$E_\parallel = \mathcal{D}_\parallel = -\left\langle \frac{1}{c}\boldsymbol{v}_1 \times \boldsymbol{B}_1 \right\rangle_\parallel$$
$$= -\left\langle \frac{(\boldsymbol{E}_1 \times \boldsymbol{B}) \times \boldsymbol{B}_1}{B^2} \right\rangle_\parallel, \tag{6b}$$

where $\boldsymbol{E}_1$, $\boldsymbol{B}_1$, and $\boldsymbol{v}_1$ are 3D fluctuations around the mean fields due to kink modes driven by the jet current, and for MHD we drop the term $f_1\boldsymbol{E}_1$, leaving $\boldsymbol{v}_1 \times \boldsymbol{B}_1$ with $\boldsymbol{v}_1 = \int d\boldsymbol{p}\left(\frac{f_1\boldsymbol{u}}{n}\right)$. Equation 6(b) can be rewritten as

$$\boldsymbol{E}_\parallel = -\langle \boldsymbol{E}_{1\perp} \cdot \boldsymbol{B}_{1\perp}\rangle\left(\frac{\boldsymbol{B}}{B^2}\right). \tag{7}$$

The main issue is whether actual 3D fluctuations correlate to produce a finite $E_\parallel$, especially for ideal kink modes argued to dominate behavior in the Central Column of astrophysical jets in Colgate et al. (2015). That Equation (7) with ideal MHD perturbations does produce a finite mean electric field was demonstrated by careful measurement during kink-mode instability in the SPHEX experiment under conditions when resistivity was negligible (al-Karkhy et al. 1993). Acceleration of ions by this electric field has been verified directly (Rusbridge et al. 1997).

Theoretical evidence that ideal MHD fluctuations can correlate is shown in Figure 2 giving just the inductive contribution to $E_\parallel$ produced by ideal MHD kink modes (McClenaghan et al. 2014), using the nonlinear non-relativistic GTC PIC code (Deng et al. 2012).
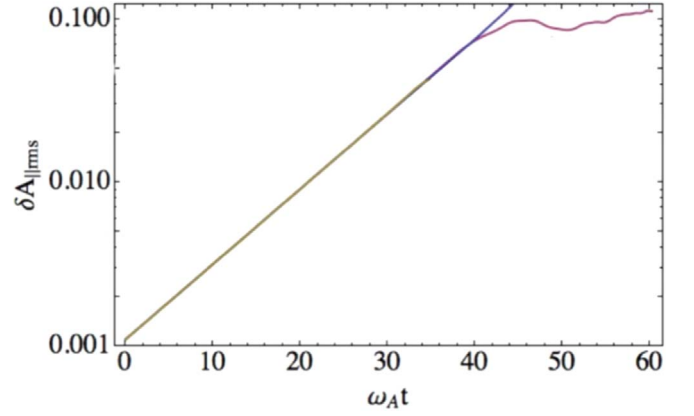
Figure 2. Showing the growth and saturation of the inductive component of the hyper-resistive electric field parallel to the magnetic field due to kink-mode turbulence in the jet Central Column in Figure 1.

3.2.1. Hyper-resistivity as Diffusion

Given favorable correlations, we estimate the magnitude of $E_\parallel$ as follows. We write $E_\parallel$ as

$$E_\parallel = -\frac{1}{c}\langle \boldsymbol{v}_1 \times \boldsymbol{B}_1 \rangle_\parallel = \eta_H j_\parallel$$
$$\approx \left(\frac{D_r^H}{ac}\right) B_a \approx \left(\frac{a}{ct}\right) B_a \approx \frac{\mathcal{V}}{ct}, \tag{8}$$

using $j_\parallel \approx \frac{cB_a}{4\pi a}$ and $\mathcal{V} \approx aB_a$ from Table 1. Equation (8) represents magnetic relaxation by hyper-resistive current diffusion (Fowler & Gatto 2007), with $\mathcal{D}_\parallel$ in Equation 5(b) giving $\eta_H = \mathcal{D}_\parallel / j_\parallel = -\langle \frac{1}{c}\boldsymbol{v}_1 \times \boldsymbol{B}_1 \rangle_\parallel / j_\parallel$ symmetrically averaged over fluctuations $\boldsymbol{v}_1$ and $\boldsymbol{B}_1$. Note that η_H has units of resistivity while $\mathcal{D}_\parallel$ (which we are calling hyper-resistivity) has units of the electric field. The term with $D_r^H = (c^2\eta_H/4\pi)$ relates hyper-resistivity to diffusion of the current, by analogy with classical diffusion via ordinary collisional resistivity. This characteristic relationship of hyper-resistivity in any direction $\boldsymbol{x}$ producing diffusion perpendicular to $\boldsymbol{x}$ will recur in considering ion acceleration by diffusion in Equation 13(b).

Ion acceleration by kink-mode driven fluctuations has also been investigated recently using particle-in-cell simulations by Alves et al. (2018). As noted in Alves et al. (2018) and Colgate et al. (2015), the strength of kink-mode acceleration depends on the available free energy (see also Section 5.1). Simulations in Alves et al. (2018) introduce strong kink drive that could account for transient acceleration (flares, etc.) near the disk. By contrast, Equation (8) predicts a weaker quasi-steady acceleration over the full length of the jet. That the net free energy driving kinks only extracts a fraction of the total jet power can be seen as follows.

All kink-mode activity is driven by a gradient in $\lambda = (4\pi/c)(j_z/B_z)$ with poloidal field B_z and current density j_z. It is known that $\lambda(r)$ has stable profiles characterized by a flattening of $\lambda(r)$ at $r < a$, where j_z is maximum, then falling toward zero at larger r (Robinson 1978; Fowler et al. 2009b). In situations like this, we expect the profile to relax toward the stable state, by flattening $\lambda(r)$ inside $r = a$. In an AGN jet, complete relaxation is prevented by the steady input of finite $d\lambda/dr$ at the disk, the effect of which is smoothed along the jet by Alfvén velocity $v_A = c \gg dL/dt$ as the jet slows down.

In an elapsed time t, the kink-induced voltage drop is $(v_A t)(D_r^H/ac)B_a < \mathcal{V}$. For $\mathcal{V} = aB_a$ and $v_A = c$ from Table 1, this gives $D_r^H < a^2/t$. But if we take $D_r^H \approx a^2/t$, it gives the result for the accelerating electric field on the far right-hand side of Equation (8).

3.2.2. Voltage Drop in the Central Column and Curvature Radiation

We apply Equation (8) to $E_\parallel$ averaged over the duration of the jet, giving, at any elapsed time t, $L = t\left(\frac{dL}{dt}\right) = 0.01ct$ from Equation (1). Using also Equation (8), we obtain

$$\Delta\mathcal{V} = LE_\parallel \approx 0.01\mathcal{V}. \tag{9}$$

That this $\Delta\mathcal{V}$ is independent of the elapsed time t is a result of localization of internal kink modes to $k_z a \approx 1$ (Colgate et al. 2015). Then, even if the disk current profile itself does not relax, within a few wavelengths the local effect of internal kink modes can cause the jet current profiles to relax toward a stable state. As the system evolves nonlinearly, instability growth rates and D_r^H diminish as the current density approaches this stable profile. Then, the longer the duration, the weaker is the time-averaged D_r^H needed to spread the current toward a stable profile. Implicit in this argument is the slow evolution of the $\lambda(r)$ profile driving kink instability, on the accretion $\dot{M}$ timescale τ, which is also the lifetime of the jet.

The $\Delta\mathcal{V}$ in Equation (9) represents dissipation in the Central Column that depletes the power available to accelerate ions to UHECR energies, but only slightly because of the large inductance giving the slow evolution of the jet length, $\frac{dL}{dt} = 0.01c$. The dissipation is in the form of acceleration of electrons giving the correct power for observed synchrotron radiation, in Section 5, and ion acceleration that is also mostly dissipated as radiation due to charged particles following the curvature of twisted magnetic field lines. By Equation 6(a), the maximum energy allowed by curvature radiation is given by $E_\parallel = E_{RAD}$ with (Jackson 1998, Equation (14.31))

$$E_{RAD} = \frac{2}{3}e\alpha_C^2\left(\frac{\beta_L\gamma_L}{c}\right)^4. \tag{10}$$

Here the right-hand side gives the radiation with $\alpha_C = \frac{c^2}{R_C}$ for relativistic ions or electrons following field lines with curvature radius R_C for which the Lienard factor $\beta_L = 1$. The maximum Lorentz factor γ_L allowed by $E_\parallel = E_{RAD}$ is independent of particle mass, given by

$$\gamma_L \leqslant \left(\frac{3E_\parallel R_C^2}{2e}\right)^{1/4}, \tag{11a}$$

$$\gamma_{CC} = 3.4 \times 10^7 M_8^{5/8}. \tag{11b}$$

The energy $E_a = m_i c^2 \gamma_{CC}$ is achieved in a length $(E_a/e\Delta\mathcal{V})$ $L \approx 10$ kpc. To get γ_{CC}, we have used Equation (10) with $E_\parallel = 0.01\mathcal{V}/L$ by Equation (9), line curvature $R_C = a$, and parameters in Table 1. A few ions at $R_C = r < a$ have $\gamma_L > \gamma_{CC}$. Note that γ_{CC} representing the maximum acceleration energy in the Central Column is far below $\gamma_L \approx 10^{11}$ (or 10^{20} eV) required to explain UHECRs—hence the need for additional acceleration in the nose. On the other hand, that the Central Column is otherwise an excellent accelerator follows from a calculation of the ion Larmor radius $r_L = v_\perp/\Omega_{ci}$ and

pressure parameter β_{CC} in the Central Column, giving

$$\beta_{CC} = \frac{8\pi n_i m_i \gamma_L c^2}{B_a^2} = \frac{4r_{L0}}{a} \ll 1, \tag{12a}$$

$$\left(\frac{r_{L0}}{a}\right)_{CC} \equiv \frac{m_i \gamma_{CC} c^2}{aeB_a} = 2.5 \times 10^{-4} M_8^{1/8} \ll 1, \tag{12b}$$

$$(r_L)_{CC} = \frac{v_\perp}{\Omega_{ci}} = r_{L0}\left(\frac{v_\perp}{c}\right), \tag{12c}$$

where in Equation 12(c) $\boldsymbol{v}_\perp$ is the ion velocity. In Equation 12(a) the numerator is the ion energy and we use the density $n_i = n_I = \frac{I}{e\langle v\rangle A}$ with $\langle v\rangle \approx c$, $A = \pi a^2$ and I in Table 1, and in Equation 12(b) we use $\Omega_{ci} = \frac{eB}{m_i\gamma_L c}$ with $B = B_a$ at $r = a$ and $\gamma_L = \gamma_{CC}$ in Equation 11(b). We see that the low β_{CC} giving strong magnetic collimation is coincident with small $\frac{r_L}{a}$ giving good ion confinement.

That ions in the Central Column should run away to the energy in Equation 11(b) and that these runaway ions carry most of the current is shown as follows. Briefly, for $\Delta\mathcal{V}$ from Equation (9) with numbers from Table 1, both ions and electrons reach a maximum $\gamma_L = \gamma_{CC}$ at a distance $0.02L$. But two-stream instability between the oppositely accelerated relativistic ions and electrons spreads electron momentum between $-\gamma_{CC}m_e c < p_{\parallel e} < +\gamma_{CC}m_e c$. As shown in Appendix B, this kills the electron current, while by momentum conservation the corresponding ion momentum spread is less by a factor m_e/m_i so that the ion distribution is approximately a delta-function around $p_{\parallel i} = \gamma_{CC}m_i c$ carrying current at speed c. Details of two-stream instability are discussed in Appendix B.2.

3.3. Ion Acceleration in the Nose

We now consider the particle acceleration at the end of jets (i.e., the nose region where the jet magnetic field and current turn to the radial direction). Internal kink instability due to j_z occurring in the Central Column, as analyzed in Colgate et al. (2015) and used in Section 3.2, should persist for some distance into the nose driven by j_r as the current turns radially in the nose, now less affected by curvature radiation as B_ϕ falls like $1/r$ giving curvature parameter $\alpha_C \propto 1/r$. But a new acceleration mechanism arises due to conditions in the nose region different from those in the cylindrical Central Column. One new condition concerns the sensitivity of the curvature radiation, Equation 11(a), to R_C that allows ions to be accelerated to the full voltage $\mathcal{V}$ in the nose region, where $R_C = r$ becomes large. Another new condition concerns the escape of ions from the nose, escape itself turning out to be a necessary ingredient for the powerful acceleration mechanism not present in the Central Column.

There are two ways that ions can escape from the nose. First, while ion orbits are magnetically confined in the Central Column, in the absence of an electric field ion orbits in the nose are not confined due to drifts of guiding centers in z caused by the curvature of field lines and gradients in the magnetic field intensity. Opposite drifts by electrons establish an electric charge giving $E \propto T_e$, the electron temperature, which can cause ions to escape by $\boldsymbol{E} \times \boldsymbol{B}$ motion. In addition, ions can also escape by hyper-resistive diffusion, which is what we will mainly discuss.

3.3.1. Hyper-resistive Diffusion in the Nose

As in Section 3.2.1, we represent hyper-resistivity in the nose as diffusion, noting that an electric field larger than that produced by charge separation is created if turbulence in the nose causes ions to escape by diffusion. To see this, consider the radial component of the relativistic Ohm's law in Equations 5(a). In the nose, $\boldsymbol{j} \times \boldsymbol{B} = \underline{z}(j_r B_\phi - j_\phi B_r)$ with unit vector $\underline{z}$, and electron flow $\boldsymbol{v}_e$ is either that due to drifts in the z-direction or that parallel to $\boldsymbol{B}$ giving $v_{er} < \left(\frac{B_r}{B}\right)c$ so that we can drop the relativistic correction to E_r. Applying Equation 5(a) in the r-direction (perpendicular to $\boldsymbol{B}$) gives

$$E_r = -\frac{1}{c}\frac{\partial A_r}{\partial t} - \frac{\partial \Phi}{\partial r} = \frac{1}{c}v_z B_\phi + \mathcal{D}_r, \qquad (13a)$$

$$(E_r)_{\mathrm{accl}} = -\frac{\partial \Phi}{\partial r} = \frac{1}{c}\left(\langle v_z\rangle - \frac{dL}{dt}\right)B_\phi + \frac{\langle D_z^H\rangle}{c\Delta}B_\phi, \qquad (13b)$$

$$\int_a^R dr (E_r)_{\mathrm{accl}} = f_{\mathrm{conv}}(\mathcal{V} - \Delta\mathcal{V}) \approx f_{\mathrm{conv}}\mathcal{V}. \qquad (13c)$$

Equation 13(b) giving the cosmic-ray accelerator $(E_r)_{\mathrm{accl}}$ is obtained as follows. Early in jet propagation when $\mathcal{D} = \boldsymbol{0}$ in the jet and nose, all of the voltage drop in the jet (giving net zero voltage around the loop) can be approximated as $-\frac{1}{c}\frac{\partial A_r}{\partial t} = \frac{1}{c}v_z B_\phi = \left(\frac{1}{c}\frac{dL}{dt}\right)B_\phi$, which appears as an inductive electric field in our disk-centered reference frame. It is this inductive field that serves to buildup B_ϕ behind the nose advancing at velocity $\frac{dL}{dt}$. Even as the jet slows down, it continues to be true that it is $-\frac{1}{c}\frac{\partial A_r}{\partial t} = \left(\frac{1}{c}\frac{dL}{dt}\right)B_\phi$ that builds up B_ϕ, giving Equation 13(b) with $\left(-\frac{\partial \Phi}{\partial r}\right)$ in our reference frame serving as the cosmic-ray accelerator in the nose. The final step relates the radial hyper-resistivity $\mathcal{D}_r$ to vertical hyper-resistive diffusion $\langle D_z^H\rangle$ that ejects ions in the z-direction, analogous to radial kink-mode diffusion producing $E_\parallel$ in Section 3.2.1. Here $\langle D_z^H\rangle$ is averaged over the energies of escaping ions, and Δ is the flux width in the nose. The nose-averaged vertical velocity $\langle v_z\rangle$ is dominated by nose ions giving $\langle v_z\rangle \approx dL/dt$ and $(E_r)_{\mathrm{accl}} \approx (\langle D_z^H\rangle/c\Delta)B_\phi$, which shows that it is the escape of cosmic rays vertically that drives cosmic-ray acceleration radially (as weak radial escape drives vertical acceleration in the Central Column). The $(E_r)_{\mathrm{accl}}$ in Equation 13(b) adds to any residual $E_\parallel$ due to kink modes in the nose as field lines bend radially to create the nose, giving a continuous B_ϕ while B_z turns into B_r. Equation 13(c) relates $(E_r)_{\mathrm{accl}}$ in the nose to the kinetic conversion (acceleration) efficiency f_{conv}, aside from $\Delta\mathcal{V} \approx 0.01\,\mathcal{V}$ due to kink acceleration, in Equation (9), which we neglect here.

3.3.2. DCLC Instability

The origin of the cosmic-ray accelerator field $(E_r)_{\mathrm{accl}}$ is not yet specified. Strong diffusion giving a large $(E_r)_{\mathrm{accl}}$ would inevitably arise due to the DCLC instability (Post & Rosenbluth 1966), known from fusion research. Like the two-stream instability discussed in Section 3.1, DCLC is a kinetic effect, not in MHD theory. Like two-stream, it involves energy of an ion beam driving plasma waves due to electrons. For two-stream, the wave vector $\boldsymbol{k}$ is parallel to $\boldsymbol{B}$ and the

frequency is the (relativistic) electron plasma oscillation frequency. For DCLC, $\boldsymbol{k}$ is perpendicular to $\boldsymbol{B}$ and the wave is an electron "drift wave" resonant with ion cyclotron motion. A dispersion relation valid both for two-stream and DCLC has the following form (derived in Appendix B):

$$1 - F_i(\omega, \boldsymbol{k}) = \left(\frac{k_\parallel^2}{k^2}\right)\left(\frac{\omega_{pe}^{*\,2}}{\omega^2}\right) + \left(\frac{k_\perp^2}{k^2}\right)\left(\frac{\varepsilon}{k}\right)$$
$$\times \left(\frac{\omega_{pe}^2}{\omega_{ce}\omega}\right) + \frac{r_{\mathrm{Li}}}{\Delta}\left(\frac{1}{k_\perp r_{\mathrm{Li}}}\right)\left(\frac{\omega_{pe}^2}{\omega_{ce}\omega}\right), \qquad (14)$$

where $\omega_{pe}^* = (4\pi ne/m_e\gamma_{\mathrm{Le}}^3)^{1/2}$ (see Equation (50)) and $\omega_{pe}^2/\omega_{ce}\omega$ is independent of electron mass; $k_\parallel$ and $k_\perp$ are components parallel and perpendicular to $\boldsymbol{B}$; and $F_i(\omega, \boldsymbol{k})$ is the ion term derived in Appendix B. In the Central Column, initially the dominant electron waves are plasma oscillations with $k_\perp = 0$ on the right-hand side. This is the two-stream instability that we found not to affect ions very much, mentioned in Section 3.2. But as ions enter the nose, new conditions allow the ions to excite electron "drift waves" giving DCLC instability resonant at the ion cyclotron frequency. Drift waves are caused by the electron density gradient given in the nose by $\varepsilon \equiv \frac{dn}{dz}/n = \frac{1}{\Delta}$. Why and when drift waves produce DCLC instability can be understood as follows.

It is useful to begin with a situation in which an ion beam cannot drive DCLC instability. Consider a straight ion beam embedded in a uniform magnetic field B_z. Let the beam be described by a distribution function $\exp[-m_i(p_z - p_{\mathrm{beam}})^2/2T]$, with thermal electrons at rest. The relative momentum $p_z = p_{\mathrm{beam}}$ can drive two-stream but not DCLC. Now add a current giving a field B_ϕ. For small ion Larmor radii, the ion beam now follows a twisting path produced by the combination of B_ϕ and B_z. As explored in the following discussion, ions following the bending field lines into the nose experience a centrifugal force that causes them to acquire a minimum $p_\perp = (r_{L\,0}/a)p_\parallel$, giving then a hole in the relativistic momentum distribution $f(p_\perp) = \int dp_\parallel f(p_\perp, p_\parallel)$ that provides the free energy driving DCLC in jet/lobe structures. This $p_\perp$-free energy still drives DCLC after Landau damping has killed all modes with finite $k_\parallel$, as was first discovered in fusion mirror machines driven unstable by an electrostatic ejection of cold ions inherent in those devices (Fowler 1981).

The ion resonance giving DCLC instability only occurs for a sufficiently large value of $\frac{r_{\mathrm{Li}}}{\Delta}$, found by choosing $k_\perp$ and ω to minimize the value required to satisfy Equation (14). This yields the same criterion for the onset of instability as the well-documented result for the non-relativistic case if we simply replace rest masses by relativistic masses, giving a relativistic ion plasma frequency $\omega_{pi} = \left(\frac{4\pi ne^2}{m_i\gamma_{\mathrm{Li}}}\right)^{1/2}$ and a relativistic ion cyclotron frequency $\Omega_{ci} = \frac{eB_\phi}{m_i\gamma_{L_i}c}$. Then the DCLC instability occurs if $r_L/\Delta > 0.4\left(\frac{\Omega_{ci}^2}{\omega_{pi}^2}\right)^{2/3}$ (Post & Rosenbluth 1966; Fowler 1981).

We rewrite the DCLC instability condition by eliminating Ω_{ci} using $r_L = v_\perp/\Omega_{ci} = \frac{m_i\gamma_i c^2}{eB_\phi}\left(\frac{v_\perp}{c}\right)$ with dominant field $B_\phi = 2I/r$, and by eliminating ω_{pi} using n from Table 1, giving for relativistic current carriers $n = \frac{I}{Aec} = \frac{rB_\phi}{2ecA}$ with $A = 2\pi r\Delta$ for return flux width Δ. Substituting these

quantities into the DCLC instability condition, we obtain after some algebra

$$r_L/\Delta > 0.4\left(\frac{\Omega_{ci}^2}{\omega_{pi}^2}\right)^{2/3} = 0.4\left(\frac{B_\phi^2}{4\pi n m_i \gamma_{Li} c^2}\right)^{2/3}, \quad (15a)$$

$$= 0.4\left(\frac{ecAB_\phi}{2\pi r m_i \gamma_{Li} c^2}\right)^{2/3} = 0.4[(\Delta/r_L)(v_\perp/c)]^{2/3}, \quad (15b)$$

$$\frac{v_\perp}{c} = \left(\frac{r_{L0}}{a}\right)\left(\frac{\gamma_{Li}}{\gamma_{L0}}\right), \quad (15c)$$

$$\frac{r_L}{\Delta} \geqslant 0.6\left(\frac{r_{L0}}{a}\right)^{2/5}, \quad \text{for DCLC onset in the nose}, \quad (15d)$$

where we use n from Table 1 with $\langle v \rangle \approx c$. Substituting Equation 15(b) into 15(a) gives Equation 15(c), with $\gamma_{Li} = \gamma_{L0} \equiv \gamma_{CC}$ as ions enter the nose.

Equation 15(b), with r_{L0} in Equation 12(b), is derived from the perpendicular momentum equation $\frac{dp_\perp}{dt} = (\text{Force})_\perp$, as follows. Since the two-stream instability does not scatter ions very much, the orbital spin velocity $v_\perp = (p_\perp/m_i\gamma_L)$ is determined by balancing the centrifugal force, $m\gamma_L c^2/r$, due to magnetic curvature radius r, against the restraining magnetic force, $e(v_\perp/c)B_\phi$ with $B_\phi = B_a(a/r)$. This ignores the ion synchrotron radiative force, which is much weaker, so that $v_\perp$ in Equation 15(b) is always maintained. This is the minimum $v_\perp$ required for ion confinement in a twisting magnetic field, giving then the hole in momentum space causing DCLC instability to occur.

3.3.3. Onset of DCLC Instability

Initially, the low $\beta_\perp \ll 1$ carried forward from the Central Column preserves a force free field as ions enter the nose, giving $B_z \to B_r \approx B_\phi$ as field lines bend radially in the nose with flux width $\Delta \approx a/2$, obtained from force balance $j_r B_\phi = j_\phi B_r$, which gives $B_\phi/B_r = 2\Delta/a = 1$ using $B_\phi = B_a(a/r)$ and flux conservation $B_r = \pi a^2 B_a/(2\pi r \Delta)$. Also, initially the DCLC instability condition is not satisfied at the entry to the nose. However, for parameters above and numbers from Table 1, even with no further acceleration by kink modes, the condition for DCLC instability would already be satisfied at a radius $r = R_{ac}$, where the DCLC condition in Equation 15(c) is first satisfied.

We calculate the radius R_{ac} where DCLC commences as follows. We take R_{ac} to be r at the margin of DCLC instability, satisfying Equation 15(c) with the equality sign with $r = R_{ac}$ and r_L in the nose. We obtain

$$r_L = r_{L0}\left(\frac{v_\perp}{c}\right)\left(\frac{r}{a}\right) = \left(\frac{r_{L0}}{a}\right)^2 r \quad \text{at nose}, \quad (16a)$$

$$r_L/\Delta = \frac{2r_L}{a} = 0.6\left(\frac{r_{L0}}{a}\right)^{2/5}, \quad (16b)$$

$$R_{ac}/a = (0.6/2)(a/r_{L0})^{8/5} = 1.7 \times 10^5 M_8^{-1/5}, \quad (16c)$$

$$r_L/\Delta = 2r_L/a = 0.02 M_8^{1/20}. \quad (16d)$$

Again, M_8 is M in units of 10^8 solar masses. Equation 16(a) uses Equation 15(b), and Equation 16(b) is Equation 15(c) with the equality and $\Delta = a/2$. Equation 16(c) comes from Equation 16(b) using Equation 16(a) with $r = R_{ac}$. Numerical values are from Table 1. These results follow from the fact that,

even though as ions flow into the nose scaling gives constant $v_\perp$ at its value in the Central Column until further acceleration occurs, the cyclotron frequency $\Omega_{ci} \propto B_\phi \propto 1/r$ giving $r_{Li} \propto r$ that must eventually exceed a fixed Δ in the DCLC instability condition, Equation 15(c).

3.3.4. Ion Acceleration to UHECR Energies

After the onset of DCLC instability at $r = R_{ac}$, two things happen. First, acceleration causes the ion energy E to begin to increase. Second, DCLC scattering of ions gives $v_\perp \to c$ in about one cyclotron period, too fast for ion synchrotron radiation to prevent this as it did in the Central Column. Then, using $\mathcal{V} = aB_a$ from Table 1, the relativistic ion Larmor radius in the nose becomes $r_L = (c/\Omega_{ci}) = \left(\frac{r}{aB_a}\right)\left(\frac{m_i\gamma_i c^2}{e}\right) = r(E/eV)$ with an energy distribution $f(E)$ due to downward scattering by DCLC.

At the onset of DCLC, Equation 16(d) shows that ions are still well confined within the initial flux width of the force free field. As the energy E increases by DCLC acceleration, ions would remain confined only if the flux width widens to satisfy $\Delta > r_L$ for all confined ions. The flux width also determines a pressure parameter $\beta_\perp$ giving the vertical pressure balance. We calculate $\beta_\perp$ in three steps:

$$\Delta > r_L = [m_i c^2 \gamma_L/eB_\phi(a)(a/r)] = r(E/eV), \quad (17a)$$

$$\frac{dp}{dz} = \frac{p}{\Delta} \approx -\frac{1}{c}[j_r B_\phi - j_\phi B_r] \approx -\left(\frac{1}{8\pi\Delta}\right)[B_\phi^2 - B_r^2], \quad (17b)$$

$$\beta_\perp = (8\pi p/B_\phi^2) = 1 - (B_r^2/B_\phi^2) = 1 - \left(\frac{a}{2\Delta}\right)^2. \quad (17c)$$

Equation 17(b) uses $(4\pi j/c) = \nabla \times \boldsymbol{B}$. Dividing Equation 17(b) by $(B_\phi^2/8\pi\Delta)$ gives Equation 17(c). The far right-hand side of Equation 17(c) uses flux conservation to write $2\pi r\Delta B_r = \pi a^2 B_a = \pi a r B_\phi$ giving $B_r/B_\phi = (a/2\Delta)$.

Thus the onset of DCLC changes the dynamics in the following sequence: DCLC acceleration sets in at $r > R_{ac}$; the Larmor radius r_L increases to equal $\Delta = a/2$, the initial flux width in the nose; and any further increase in energy could cause the ions to escape. But, in trying to escape, ions attached to field lines begin to spread out the flux, causing the flux width Δ to expand so as to contain the most energetic ions. And as the flux expands, $\beta_\perp \to 1$ by Equation 17(c). Thus, in fairly short order, system variables evolve to

$$\Delta \approx (r_L)_{\text{MAX}} \approx r(E_{\text{MAX}}/e\mathcal{V}), \quad (18a)$$

$$E_{\text{MAX}}(r) \approx E_a + \int_{R_{ac}}^{r} e(E_r)_{\text{accel}} dr < f_{\text{conv}}(e\mathcal{V}), \quad (18b)$$

$$\beta_\perp \approx 1, \quad (18c)$$

where $E_a = m_i \gamma_{CC} c^2 = 3.4 \times 10^{16} M_8^{5/8}$ eV is the energy as ions emerge from the Central Column if we neglect kink-mode acceleration in the nose, and E_{MAX} is the energy of ions that enter the nose directly from the Central Column, as opposed to cold ions recycling from the ambient as discussed in Section 4.4.

At $\beta_\perp \approx 1$, field lines begin to untwist, giving $B_r \ll B_\phi$ so that the current carried dominantly by j_r can no longer flow parallel to field lines. Yet this current must be maintained to satisfy our mean-field MHD equilibrium, as the displacement

current can be ignored for this slowly evolving field, giving $\nabla \cdot \boldsymbol{j} = 0$ so that the poloidal current $j_z \to j_r$ is continuous across the nose. Because the nose ion current must flow perpendicular to the dominant field B_ϕ, as field lines untwist, a hyper-resistive diffusive transport rate $\langle D_r^H \rangle$ is required to carry the current, giving

$$j_r = -e\langle D_r^H \rangle \frac{\partial n}{\partial r} = en\langle v \rangle, \quad (19a)$$

$$\langle v \rangle = -\langle D_r^H \rangle \left(\frac{1}{n} \frac{\partial n}{\partial r} \right), \quad (19b)$$

$$j_z \text{ (Central Column)} = nec \to j_r = enc(\Delta/r) \text{ (nose)}. \quad (19c)$$

That a net ion current results in Equation 19(a) arises from the fact that $\langle D_r^H \rangle$ by DCLC turbulence represents a random walk in momentum due to ion scattering analogous to collisional scattering. Because DCLC is resonant at the ion cyclotron frequency, scattering by DCLC affects ions only but does not affect electrons. That drift waves excited by DCLC do affect both ions and electrons plays a role in vertical transport in and out of the nose, in Section 4.4. Finally, Equation 19(c) takes note of the transition from current density *nec* in the Central Column where current flows along field lines, to a reduction by a factor (Δ/r) when finally diffusion must transport current perpendicular to $\boldsymbol{B}$, where we anticipate $D_r^H = D_z^H = \Delta c$ from Equation 21(e) as follows.

It remains to verify that ion radiation can be neglected in the nose. We rewrite the momentum Equation (3) to apply to the nose, giving

$$\frac{dp}{dt} = m_i c^2 \frac{\partial \gamma_L}{\partial r} = e(E_r)_{\text{accel}} - \frac{2}{3} e^2 \gamma_L^4$$
$$\times \left[\left(\frac{(v_\perp/c)^4}{r_L^2} \right) + \left(\frac{1}{r^2} \right) \right], \quad (20)$$

where we approximate $\frac{d}{dt} = c\frac{\partial}{\partial r}$ and the radiation term, from Equation (10), represents both synchrotron radiation $\left(\propto \frac{1}{r_L^2} \right)$ and curvature radiation $\left(\propto \frac{1}{r^2} \right)$. Before DCLC sets in, $(v_\perp/c) = (r_{L0}/a)$ in Equation 15(b) gives synchrotron radiation equal to curvature radiation. Then, even with $(E_r)_{\text{accel}} = 0$, integrating Equation (20) gives $\gamma_L = \gamma_{\text{CC}} \Big/ \left[1 + 10^{-8} \left(1 - \left(\frac{a}{r} \right) \right) \right]^{1/3} \approx \gamma_{\text{CC}}$ for any $r < R_{ac}$ before DCLC begins. When DCLC does set in, the dominant synchrotron radiation with $(v_\perp/c) \approx 1$ is still negligible compared to DCLC acceleration approximated as $(E_r)_{\text{accel}} \approx \mathcal{V}/[r \ln(R/a)]$, giving $E_{\text{SYN}}/E_{\text{accel}} < 0.01$ near $r = R_{ac}$, decreasing as r increases.

3.4. DCLC Quasi-linear Transport, Ion Energy Distribution

We now try to calculate the likely nonlinear outcome of DCLC instability in producing the accelerated ion distribution. The nonlinear development of DCLC instability was shown to explain momentum transport in the 2XIIB mirror experiment (Berk & Stewart 1977). Later Smith & Cohen (1983) applied Kaufman's formal method (Kaufman 1972) to derive an exact quasi-linear DCLC transport equation in action-angle space, a method that can be extended to give a Fokker–Planck equation

including both diffusion and friction (Fowler & Gatto 2007). For relativistic DCLC, the important action variables are the ion magnetic moment $P_\mu = (p_r c^2/eB_\phi) = r_{\text{Li}}c$, and the radial canonical momentum $P_r = p_r + (e/c)A_r$ with $p_r = m_i \gamma_{\text{Li}} v_r$ and vector potential $A_r(r, z)$, giving $\frac{\partial A_r}{\partial z} = B_\phi$. Here we will approximate the formal results in the two-dimensional P_μ and P_r space to proceed directly to a 3D quasi-linear equation for transport in p_r, r and z, as follows.

Using D_{pr}^H to represent mean hyper-resistive diffusion in the radial component of momentum, D_μ^H as diffusion in pitch angle, D_r^H and D_z^H as spatial diffusion in radial and z directions, we obtain

$$\frac{\partial f}{\partial t} = -eE_r \frac{\partial f}{\partial P_r} + \frac{\partial}{\partial P_r} D_{pr}^H \frac{\partial f}{\partial P_r} + \frac{\partial}{\partial P_\mu} D_\mu^H \frac{\partial f}{\partial P_\mu} + S, \quad (21a)$$

$$= \frac{\partial}{\partial p_r} \left[-e(E_r)_{\text{accel}} f + D_{pr}^H \frac{\partial f}{\partial p_r} \right] + \frac{\partial}{\partial z} D_z^H \frac{\partial f}{\partial z}$$
$$+ \frac{\partial}{\partial r} D_r^H \frac{\partial f}{\partial r} + S, \quad (21b)$$

$$D_{pr}^H \approx \left\langle eE_{1r}\Omega_{ci} \int_{-\infty}^{t} dt' \, eE_{1r}(r'(t')) \right\rangle, \quad (21c)$$

$$D_z^H = D_{pr}^H \Big/ \left(\frac{\partial P_r}{\partial z} \right)^2 = (eB_\phi/c)^{-2} D_{pr}, \quad (21d)$$

$$D_r^H = D_{pr}^H/(\partial P_r/\partial z) D_\mu^H \leqslant r_{\text{Li}}^2 \Omega_{ci} \approx c\Delta. \quad (21e)$$

Here f is the distribution function of the accelerated ions, and the source S represents input from the Central Column (at energy E_a) plus recycling from the ambient discussed in Section 4.4. In Equation 21(a), the first term on the right-hand side represents ion acceleration in the nose. The other terms describe diffusion during acceleration. Equation 21(b) applies the transform to variables p_r, r, and z. For DCLC, the formal theory shows that all transport processes arise from the electrostatic perturbation E_{1r}, giving the relationships shown in Equations 21(c), (d), and (e). Though D_r^H and D_z^H turn out to be of similar magnitude, physically D_r^H derived from D_μ^H is analogous to a random walk by ion "collisions" due to cyclotron resonance, while D_z^H includes also random walk by DCLC drift-wave $\boldsymbol{E} \times \boldsymbol{B}$ motion. For strong instability with growth rate Ω_{ci}, both processes give a correlation time Ω_{ci}^{-1} with the ion Larmor radius as the step size. That r_{Li} is the step size for $\boldsymbol{E} \times \boldsymbol{B}$ motion follows from $(cE_r/B_\phi \Omega_{ci}) \approx r_{\text{Li}}$.

We approximate the solution of Equation 21(b) by

$$f(r, E) \approx n(r) \left[C^{**} \exp \int_{p_a}^{E/c} dp_r [e(E_r)_{\text{accel}}/D_{pr}^H] \right], \quad (22a)$$

$$\approx n(r) \left[C^{**} \exp \int_0^E dE'(1/E_{\text{MAX}}(r)) \right], \quad (22b)$$

$$\approx n(r)(1/1.73 E_{\text{MAX}}(r)) \exp(E/E_{\text{MAX}}(r)),$$
$$E^* < E_a < E < E_{\text{MAX}}(r). \quad (22c)$$

We will return to the meaning of E^* in Section 4.

We obtain Equation 22(a) by setting the first term in Equation 21(b) equal to zero, integrating and factoring out the ion density $n(r)$. We account for S by taking the lower integration limit $p_a = E_a/c$, to account for rapid acceleration of

recycling ambient ions up to the energy E_a of Central Column ions entering the nose. And we have set the spatial diffusion terms in Equation 21(b) ($\propto (n/e)\nabla \cdot \boldsymbol{j}$) equal to zero. In Equation 22(b), we first write $dp_r = dE/c$ for relativistic energies and then apply Equations 13(b) and 13(d), giving $(e/c)(E_r)_{\rm accel} = (e/c)(D_z^H/c\Delta)B_\phi \approx (D_{pr}^H/E_{\rm MAX})$ using also Equation 18(a) with $(\mathcal{V}/rB_\phi) \approx 1$ using $rB_\phi = aB_a$ for $B_\phi \propto 1/r$. To determine C^{**}, we note that DCLC momentum diffusion only spreads energies downward (to fill the "loss cone") so that ion energies at radius r do not exceed $E_{\rm MAX}(r)$, leading us to set $C^{**} = (1/1.73E_{\rm MAX})$ to give $\int_0^{E_{\rm MAX}} dE\,(f/n) = 1$. This downward spread of energies to achieve a state of marginal stability has been well documented in fusion mirror devices (Baldwin 1977; Smith & Cohen 1983), but $(E_r)_{\rm accel} \propto D_{pr}^H$ inhibits downward energy spread in jets. Note that the final result for $f_0(E)$ only depends on ratios of transport quantities, not their absolute value. Since radiation is irrelevant by Equation (20), Equation 22(c) that depends only on ratios of various D^H components is valid from the onset of DCLC, even though these D^H components are small, while the initial hole in $p_\perp$ space that drives DCLC is small.

4. Cosmic-ray Energy Spectrum, Intensity on Earth

In this section, we use the transport equation in Section 3.4 to compare our model with observations of UHE cosmic rays.

4.1. Cosmic-ray Energy Spectrum

In our model, cosmic rays are ejected via the D_z^H term in Equation 21(d). That this gives an energy spectrum similar to observations can be seen as follows.

Since UHE cosmic rays travel great distances, we treat AGN jet/radiolobes as point sources described by integrating the D_z^H term in Equation 21(b) over the entire volume of the nose, giving an energy spectrum $I(E)$. As several steps are required, we display them as follows:

$$I(E) = \int_{R(E)}^R 2\pi r\, dr \int_0^\Delta dz \frac{\partial}{\partial z} D_z^H \frac{\partial f}{\partial z}, \tag{23a}$$

$$\approx \int_{R(E)}^R 2\pi r\, dr \int_0^\Delta dz D_z^H (I/e\langle v\rangle 2\pi r\Delta) f_0(E) \left(\frac{\kappa^*}{\Delta^2}\right), \tag{23b}$$

$$\approx \kappa^*(I/e) \int_{R(E)}^R r\, dr \left(\frac{D_z^H}{r\langle v_r\rangle}\right) f_0(E)(e\mathcal{V}/rE_{\rm MAX})^2, \tag{23c}$$

$$= \kappa(I/e) \int_{R(E)}^R \frac{1}{r} dr\, f_0(E)(e\mathcal{V}/E_{\rm MAX})^2, \tag{23d}$$

$$f \approx n f_0(E) = (I/e\langle v\rangle 2\pi r\Delta) f_0(E), \tag{23e}$$

$$E = \int_{R(E)}^r dr\, eE_r, \tag{23f}$$

$$\kappa = \kappa^*(D_z^H/D_r^H), \tag{23g}$$

with $E_{\rm MAX}$ given by Equation 18(b).

In Equation 23(b), we approximate $\frac{\partial}{\partial z} = 1/\Delta$ together with a constant κ^* that we will use to guarantee energy conservation, discussed as follows. The lower integration limit $R(E)$ is defined by Equation 23(f), chosen to eliminate values of E not accessible by acceleration by E_r. In Equation 23(b), f is given by Equation 23(e) taken from Equation 22(c), with $n(r) = I/eA\langle v\rangle$ with area $A = 2\pi r\Delta$ for flux width Δ in the nose, as in Section 3.3.1. Taking $n_i \propto I$ follows, because DCLC only

drives ion current to maintain current continuity around the loop. In Equation 23(c), we first integrate in z to cancel one factor Δ, then substitute $\Delta = r(E_{\rm MAX}/e\mathcal{V})$ from Equation 18(a) in remaining factors. In Equation 23(d), we set $(D_z^H/r\langle v\rangle) = (D_z^H/D_r^H)$ using $\langle v\rangle = D_r^H/r$. While (D_z^H/D_r^H) can be order unity as discussed in Section 3.4, we choose to absorb (D_z^H/D_r^H) into κ^* giving here and hereafter the new fitting parameter κ in Equation 23(g).

To see that Equation 23(d) yields an approximate power law, we note that f_0 depends on $(E/E_{\rm MAX})$ and change variables from r to $Y \equiv (E/E_{\rm MAX})$, using

$$\frac{dY}{dr} = -\frac{E}{E_{\rm MAX}^2} \frac{dE_{\rm MAX}}{dr} \approx -\frac{Y}{r}, \tag{24a}$$

$$dr = -dY\,(r/Y), \tag{24b}$$

$$Y(R(E)) = 1, \quad Y(R) = E/e\mathcal{V}, \tag{24c}$$

where $\mathcal{V} = 1.4 \times 10^{20} M_8^{1/2}$ volts is the full dynamo voltage from Table 1. We now apply this transformation to Equation 23(d) with $r = R$ as the upper limit of integration and $f_0 = (1/1.73E_{\rm MAX})\exp\left(\frac{E}{E_{\rm MAX}}\right)$ from Equation 22(c). We obtain:

$$I(E) = \kappa(I/e) \int_{E/e\mathcal{V}}^1 dY\,(r/Y)\frac{1}{r}(1/1.73E_{\rm MAX})$$
$$\times (e\mathcal{V}/E_{\rm MAX})^2 \exp(Y), \tag{25a}$$

$$= \kappa(I/e)(1/e\mathcal{V})(e\mathcal{V}/E)^3 K(E). \tag{25b}$$

The factor $K(E)$ is given by

$$K(E) = (1/1.73) \int_{E/e\mathcal{V}}^1 dY\, Y^2 \exp(Y)$$
$$= (2.73/1.73)\{1 - [2(1 - E/e\mathcal{V}) + (E/e\mathcal{V})^2]$$
$$\times \exp[-(1 - E/e\mathcal{V})]\}. \tag{26}$$

The dominant scaling factor $1/E^3$ in Equation 25(b) arises naturally from diffusion across a flux width $\Delta \propto E_{\rm MAX}$ and the normalization of $f_0(E) \propto E_{\rm MAX}^{-1}$, together with the change of variable whereby an integration in r from $R(E)$ becomes an integration in Y from $E/e\mathcal{V}$. Then $(1/E_{\rm MAX}^3) = (Y^3/E^3)$.

4.2. The Fitting Parameter κ

We determine the fitting parameter κ by energy conservation. We delay discussion of the physical significance of κ to Section 4.4.

Neglecting the small power dissipated in the Central Column (1% by Equation (9)), the conservation of the jet power escaping as cosmic-ray ions is given by

$$f_{\rm conv} I\mathcal{V} \geqslant \int_{E^*}^{e\mathcal{V}} dE\, EI(E)$$
$$= \int_{E^*}^{e\mathcal{V}} dE\, e\mathcal{V}(E/e\mathcal{V})[\kappa(I/e)(1/e\mathcal{V})(e\mathcal{V}/E)^p]$$
$$= \kappa I\mathcal{V}(p - 2)^{-1}[(e\mathcal{V}/E^*)^{p-2} - 1], \tag{27}$$

$$\kappa = \{(p - 2)/[(e\mathcal{V}/E^*)^{p-2} - 1]\}f_{\rm conv}, \tag{28}$$

where we have approximated $(1/E^3)K(E) \approx (1/E^p)$, and the value of E^* is discussed in Section 4.3. Following

Cronin (1999), hereafter we take $p = 3$ as the basic scaling of the cosmic-ray source, our $K(E) \to 0$ at $E = e\mathcal{V}$ being an artifact of $f_0(E)$ going to zero there.

We estimate the conversion efficiency f_{conv} as follows. We define $f_{\text{conv}} = E_{\text{MAX}}(R)/e\mathcal{V}$ from Equation 18(b) at $r = R$, with $E_{\text{MAX}}(R) = \int_{R_{ac}}^{R} dr\, e(E_r)_{\text{accl}} = \int_{R_{ac}}^{R} dr\, e(D_z^H/c\Delta)B_\phi$ with $(E_r)_{\text{accl}}$ from Equation 13(b). Next, we introduce $B_\phi = B_a(a/r) = \mathcal{V}/r$ using $aB_a = \mathcal{V}$ from Table 1, and we write $\Delta = r(E_{\text{MAX}}(r)/e\mathcal{V}) \leqslant rf_{\text{conv}}$ using Equation 18(a) and the definition of f_{conv}. We obtain

$$f_{\text{conv}} = E_{\text{MAX}}(R)/e\mathcal{V} = \int_{R_{ac}}^{R} dr\, e(D_z^H/c\Delta)(B_\phi/e\mathcal{V}) \geqslant f_{\text{conv}}^{-1}$$
$$\times \int_{R_{ac}}^{R} dr(D_z^H/cr^2), \quad (29a)$$

$$f_{\text{conv}} \geqslant \left[\int_{R_{ac}}^{R} dr(D_z^H/cr^2)\right]^{1/2} \approx (D_z^H/cR_{ac})^{1/2} \approx 0.5. \quad (29b)$$

While Equation 29(b) gives the sense of what determines f_{conv}, the numerical value is justified by the reasonableness of estimates in Table 2 using parameters in Table 1 (e.g., $a \propto 1/f_{\text{conv}}$ and $a\Omega_a/c \propto f_{\text{conv}}^{1/2}$).

4.3. Calibrating the Model I(E) to Observations

Our $I(E)$ in Equation 25(b) depends on E^* through κ in Equation (28). The parameter E^* is actually determined by DCLC turbulence. Here we estimate what E^* needs to be to fit observations.

We compare our $I(E)$ with Figure 1 in Cronin (1999). This curve translates the count rate on Earth to an intensity proportional to our $I(E)$. As Cronin notes, like our $I(E)$, the basic scaling is $(1/E^3)$, then reducing to $(1/E^{2.7})$ at higher energies, perhaps for other reasons mentioned by Cronin. Cronin conveniently relates the plotted intensity to count rate above a specified energy giving $I_1 \propto \int_{E_1} dE\, I(E) \propto (1/E_1^2)$ for $I(E) \propto (1/E^3)$. This gave $(1/\text{km}^2 \text{ year})$ for cosmic rays above about 5×10^{18} eV. The same scaling correctly predicted later results giving $(1/\text{km}^2 \text{ century})$ above 6×10^{19} eV for extragalactic sources detected at the Pierre Auger Observatory (Pierre Auger Collaboration 2007, 2014, 2017). Applying Cronin's scaling to our model gives for a single AGN source,

$$I_1(E_1) = \int_{E_1}^{e\mathcal{V}} dE\, I(E) = \int_{E_1}^{e\mathcal{V}} dE[\kappa(I/e^2\mathcal{V})(e\mathcal{V}/E)^p]$$
$$= (I/e)(\kappa/(p-1))[(e\mathcal{V}/E_1)^{p-1} - 1], \quad (30)$$

where I_1 is the ion flow rate for all energies $> E_1$, with I and $\mathcal{V}$ from Table 1. That $I_1 > I/e$ implies both electron and ion recycling to maintain charge neutrality and a net disk current I as required by $\nabla \cdot \boldsymbol{j} = 0$. Recycling with the ambient is discussed in Section 4.4.

In terms of I_1, points on Cronin's curve for AGNs at a distance R_S correspond to a flux on Earth equal to $(I_1/4\pi R_S^2)$. To compare with the Pierre Auger result noted previously, we take $E_1 = 6 \times 10^{19}$ eV (Pierre Auger Collaboration 2007). Summing over N sources gives (for $p = 3$)

$$\sum_{n=1}^{N} (I_1(E_1)/4\pi R_S^2)_n = 1/(\text{km}^2 \text{ century}), \quad (31a)$$

$$0.1 < (E^*/E_a)M_8^{13/8} < 1.0. \quad (31b)$$

The range in E^* in Equation 31(b) corresponds mainly to the range in R_S, from the closest to the most distant AGNs accessible at the Pierre Auger Observatory (470 AGNs within a 240 Mlyr range, Pierre Auger Collaboration 2007). As examples, the lower limit in Equation 31(b) would correspond to a single nearby source ($N = 1$, $R_S = 10$ MPc) and the upper limit corresponds to several distant sources ($N = 10$, $R_S = 100$ MPc).

How E^* in our model can be consistent with Equation 31(b) concerns density profile adjustments to maintain marginal stability to DCLC. We employed marginal stability to determine the onset of DCLC by taking the equality in Equation 15(c) for ions of energy E_a entering the nose from the Central Column. The onset of DCLC causes the plasma pressure parameter $\beta_\perp$ to grow.

As $\beta_\perp$ grows, the field inside the nose decreases as $(1 - \beta_\perp)^{1/2}$, giving a lower DCLC threshold energy E^* given by

$$(E^*/E_a) = (1 - \beta_\perp)^{1/2}. \quad (32)$$

Equation (32) could accommodate Equation 31(b), depending on the uncertain value of $\beta_\perp$ near the DCLC onset at $r = R_{ac}$. More accurate determinations of DCLC marginal stability and the role of an additional Alfvén Ion Cyclotron (AIC) instability occurring at high $\beta_\perp$ are discussed in Fowler (1981) using non-relativistic theory, giving with relativistic masses the same results as relativistic theory, as in the case of DCLC (see Appendix B.1).

4.4. Recycling with the Ambient

AGN jets eject many more ions than those reaching the Earth as cosmic rays. In our model, the total ion ejection rate, $\int dE I(E)$, also exceeds ions entering the nose from the jet, given by I/e. The difference must be ions entering the nose from the ambient, mainly ambient plasma pushed forward by the jet nose itself. We refer to this ion injection from the ambient as Recycling, given by Equations 33(a) and (b),

$$I_{\text{RECYCLE}} = e\int_{E^*}^{e\mathcal{V}} dE\, I(E) - (I/e) \approx (I/e)\left(\frac{\kappa}{p-1}\right)$$
$$\times [(e\mathcal{V}/E^*)^{p-1} - 1] \approx (I/e)\left[\frac{1}{2}f_{\text{conv}}(e\mathcal{V}/E^*)\right], \quad (33a)$$

$$P_{\text{CR}}(r) = \int_{E^*}^{E_{\text{MAX}}(r)} dE\, EI(E) = I\mathcal{V}(f_{\text{conv}}E_{\text{MAX}}(r)/e\mathcal{V}). \quad (33b)$$

In Equation 33(a), we use κ from Equation (28). Equation 33(b) gives the distribution of cosmic-ray power P_{CR} across the radial profile of the jet nose.

We note that the necessity for recycling is characteristic of a decreasing power law (C/E^p). An excess of ions beyond that needed to conduct the jet current I results for any specified total power $I\mathcal{V}$ applied to the conservation of energy (to calibrate C), then applied to the conservation of particles (giving $I_{\text{REC}} \approx (I/e)[(p-2)/(p-1)][(\mathcal{V}/E^*) - 1]$). Our model makes this quantitative by showing that the $(1/E^3)$ power law is characteristic of a single AGN source whose black hole mass M, together with angular momentum conservation,

determines all jet parameters in Table 1. Then the total emission of extra-galactic cosmic rays includes some reaching Earth, some not.

We note also that the ambient can sustain recycling and recycling does not appear to change our model parameters. Physically, recycling is part of DCLC vertical transport, whereby adjustments in the Vlasov distribution functions $\partial f(x, p)/\partial z$ for hot ions, ambient ions, and electrons do in detail what adjusting κ does in our model. Thus recycling commences where DCLC commences, at $r = R_{ac}$ in Equation 16(c). Because of the low jet density in Table 1, snow-plowing an ambient density $n_{amb} \approx 0.01 n_{jet}$ over an annular width $\delta r < R_{ac}$ at R_{ac} would be sufficient to accommodate the result in Equation 33(a). The jet density n in Table 1 already includes recycling, any excess being expelled vertically by DCLC diffusion D_z^H to maintain just the ion density needed to conduct the current sustained by radial DCLC diffusion D_r^H. Nor would recycling add much to ambient pressure, the ratio being $[(nE)_{RECYCLE}/(n_{amb} m_i (dL/dt)^2] < 1$ using $n_{RECYCLE} \approx (10^5 I/ec\pi R^2) \approx 100 n_{amb}(a/R)^2 \approx 10^{-15} n_{amb}$ and $m_i(dL/dt)^2 = 10^5$ eV, with $(a/R)^2 \approx 10^{-17}$.

5. Electromagnetic Signatures of the Model

The synchrotron radiation by which AGN jets are made visible can, in principle, provide four signatures of our cosmic-ray model. Our model is distinctly different from shock models of synchrotron radiation. The signatures suggested here could help distinguish between these models.

First, while it has usually been assumed that a glowing radiolobe must be more or less uniformly filled with a source of radiation, our spheromak-based model of magnetic jets should produce radiation in thin magnetic filaments with magnetic field strength comparable to that near the black hole (Colgate et al. 2015). VLBA measurements do indicate filaments (R. C. Walker 2015, private communication). Better resolution could help validate our magnetic structure model.

Second, as a corollary, it is observed that synchrotron radiation has associated with it Synchrotron Self Compton (SSC) scattering to TeV gamma-ray frequencies (Krolik 1999; Li & Kusunose 2000). Filamentary SSC would further validate the model.

Third, a signature already available is existing evidence of a bright cone of synchrotron radiation on the axis of jet symmetry, with an apparent "opening angle" of about 0.01 radians (Colgate et al. 2015). This is consistent with the diffusive spreading of magnetic fields along the jet.

Finally, in trying to escape, cosmic rays can heat ambient electrons to very high energies beyond the jet/lobe region, producing radiations yet to be explored.

5.1. Electron Synchrotron Model

The two main features of our synchrotron model are (1) angular momentum conservation, which serves to project the magnetic field pattern at the disk all along the jet so that Central Column parameters at the disk determine synchrotron wavelengths; and (2) plasma turbulence, which spreads this field projection over an ever-widening cone, finally expanding into giant radiolobes like the volume enclosed by return current in Figure 1.

As noted earlier, what causes some field lines to wander away from the Central Column is MHD kink instability. As is explained in Colgate et al. (2015), there are two distinct kinds of MHD kink modes driven by the jet current, confirmed in MHD simulations (e.g., Tchekhovskoy & Bromberg 2016). In Colgate et al. (2015), we derived the two kinds of kink modes from the MHD energy principle, giving the free energy for magnetic perturbations of the form $\delta W \propto \int r \, dr \, \boldsymbol{\xi} \cdot (\boldsymbol{j}_1 \times \boldsymbol{B} + \boldsymbol{j} \times \boldsymbol{B}_1)$, where subscript 1 denotes perturbations and $\boldsymbol{\xi} \propto \exp i[m\phi + kz]$ is a displacement of magnetic field lines.

Internal kink modes with $ka \approx 1$ localized to the Central Column create the well-understood kink-mode accelerator in Section 3.2. Internal kink modes are characterized by magnetic resonances in δW. External-kink modes of interest here are those with k small enough to avoid these resonances, also dominated by $m = 1$ describing a rigid body motion of the entire magnetic structure. Because accretion disk power is concentrated near $r = a$, ξ should be thought of as arising at $z \approx 0$, $r \approx a$, growing not in time but in z along the jet length; and relativistic effects give "secular," not exponential, growth, giving $\xi \propto z$ (see Section 5.4).

Thus we come to a picture of the synchrotron radiator localized to the Central Column together with an array of magnetic field lines bounded by a conical volume of radius a near the black hole and growing like ξ along the jet. We will be able to predict the synchrotron power and dominant wavelengths without detailed knowledge of the wandering field line structure. The power is known from the calculation of the voltage drop in Equation (9). The magnetic field strength determining synchrotron wavelengths can be determined by angular momentum conservation, as follows.

Angular momentum projects the dynamo field forward, as it does in our collimated jet solution in Colgate et al. (2015). Kink instability is initiated as a bending and twisting of the jet as a whole ($m = 1$ perturbation, Hooper et al. 2012). That this preserves $B_z = B_a$ follows from a WKB solution [setting $a(\partial/\partial z) = B_r = 0$ in $\boldsymbol{j} \times \boldsymbol{B} = \boldsymbol{0}$], giving the same jet displaced in r by a path $R(\phi, z)$. Equivalently, angular momentum flow gives (Blandford & Payne 1982)

$$\frac{d}{dt} \int_0^z dz' \frac{rE_r B_z}{4\pi c} \approx \frac{rB_\phi B_z}{4\pi} = (P_{POYN}/\Omega)_{disk}, \qquad (34)$$

where we extend the meaning of dz to include wandering field lines.

Equation (34) shows that the WKB solution is like Poynting flow along a twisting light pipe. That $m = 1$ continues to dominate the nonlinear solution (even as higher m's representing filamentation appear) was shown in MHD simulations giving an $m = 1$ perturbation of the order of the mean field ($B_1 = 0.4 B_0$ in quasi-steady state, Carey et al. 2011). This corresponds to an external-kink free energy $\delta W \propto a^2 B_a^2$. Dividing an external-kink-mode current I into N filaments closely packed inside a radius a still gives $B = B_a$. Dividing the current into N filaments isolated from each other would give $(\delta W)_N \propto N(a B_a/N)^2 = (1/N)a^2 B_a^2$ and a correspondingly weaker synchrotron radiation in radiolobes not consistent with observations. This suggests that kinking current mainly follows a tube of radius a twisting along the path $R(\phi, z)$ that may fold $(c/dL/dt) = 100$ times inside the radiolobe.

The current path $R(\phi, z)$ would also be the path of most of the electrons emitting synchrotron radiation in radiolobes. We conclude that, although the mean-field B_ϕ falls off as $1/r$ outside $r > a$, the total field $B \approx B_0 + \delta B_\phi \approx B_a$ wherever most of these electrons flow, yielding the wavelength distribution in Section 5.3. Also B_1 of order B_0 was confirmed

in the tower-like MHD simulations in Carey et al. (2011), giving $B_1 = 0.4B_0$ in quasi-steady state. We have ignored the buildup of flux-amplifying closed structures, as in certain fusion devices, negligible for astrophysical jets in which helicity injection by the accretion disk is mainly consumed in lengthening the jet (Fowler et al. 2009a).

5.2. Synchrotron Luminosity

The synchrotron radiation described in Section 5.1 dissipates a large part of the electron energy produced by kink-mode acceleration in the Central Column. Electron acceleration is equal and opposite to ion acceleration in Section 3.2, giving $\frac{1}{2}I\Delta\mathcal{V} \approx 0.005I\mathcal{V}$ as the synchrotron power, or luminosity, in good agreement with observations (Krolik 1999). The synchrotron power is given by I and $\mathcal{V}$ in Table 1, yielding

$$P_{\mathrm{SYN}} \leqslant \frac{1}{2}I\Delta\mathcal{V} \approx 0.005I\mathcal{V} \approx 1.5 \times 10^{43}M_8 \text{ erg s}^{-1}, \quad (35)$$

where the inequality calls attention to this estimate as the upper limit set by jet power, not a specific calculation of radiation, though this limit is generally consistent with observations of powerful AGN jets (Krolik 1999).

5.3. Synchrotron Wavelengths

As noted previously, a new feature of our model is that, both in the Central Column and in the surrounding structure, synchrotron radiation should always be calculated using the magnetic field $B_a = 1500M_8^{-1/2}$ Gauss at $r = a$ near the black hole. Then, wherever they occur, the frequency ν and wavelength λ for synchrotron emissions at the nth harmonic are given by

$$\nu = n(eB_a/2\pi m_e c\gamma_{\mathrm{Le}}) = 4 \times 10^9(n/\gamma_{\mathrm{Le}})M_8^{-1/2} \text{ Hz}, \tag{36a}$$

$$\lambda = (c/\nu) = 7(\gamma_{\mathrm{Le}}/n)M_8^{1/2} \text{ cm}, \tag{36b}$$

with numbers from Table 1.

For a given electron energy $m_e c^2\gamma_{\mathrm{Le}}$, radiation intensity is spread over a range of frequencies around the fundamental $n = 1$ (Jackson 1998, Equation (14.31)), the total radiation for all harmonics being that given by Equation (10) applied to electron cyclotron orbits in a magnetic field. Observed radiation can be found by integrating the radiation at a fixed γ_{Le}. An example of this procedure for an assumed energy distribution is given in Li & Kusunose (2000).

We predict an upper limit on electron energies >TeVs due to curvature radiation in the Central Column, giving in Equation 11(b) $\gamma_{\mathrm{L}} = \gamma_{\mathrm{CC}} = 3.4 \times 10^7 M_8^{5/8}$ both for electrons and ions in the Central Column. Our estimate of lower ion energies outside the Central Column, in Section 5.4, suggests the same for electrons.

5.4. Synchrotron Opening Angle

As was mentioned in the introduction to this section, the wandering of field lines due to external MHD kink modes produces both field lines penetrating deeply into radiolobes and also a more compact structure often producing a bright cone along the jet axis of symmetry. We calculate the opening angle of this cone as follows. As in accelerator beam propagation, we treat external kinks as a source of beam divergence, due to

perturbations originating around $r = a$ in the disk where gravitational power is concentrated. This beam divergence grows in z so that d/dt translates to d/dz. We estimate the conical opening angle $\Theta = (\xi(z)/z)$ by interpreting $\xi(z)$ as the outer radial boundary of a fluid perturbation velocity $\boldsymbol{v}_1(\boldsymbol{x}) = -i\omega\xi(\boldsymbol{x})$. Here $\xi(\boldsymbol{x})$ is approximately constant between $R_1(z) < r < R_2(z)$, leading us to approximate unstable growth as $d\xi(z)/dt \approx dR_2/dt \approx \omega_{\mathrm{A}}\xi(z)$ with relativistic Alfvén frequency ω_{A}. In calculating ω_{A}, we must add a random $\omega\xi(z)$ to the mean-field $\boldsymbol{v}$ in the Lorentz factor, giving $\omega_{\mathrm{A}} \propto 1/\sqrt{m\gamma} \propto 1/[(1/\gamma_0^2) - (\omega_{\mathrm{A}}\xi/c)^2]^{1/2}$ with $\gamma_0 = (1 - v^2/c^2)^{-1/2}$. Then the growth of ξ saturates as $\omega_{\mathrm{A}}\xi/c \to 1/\gamma_0$, giving $\xi = ct/\gamma_0 = (cz)/(dL/dt)/\gamma_0 \approx 100z/\gamma_0$. Dividing this by z gives Colgate et al. (2015),

$$\Theta \approx \frac{\xi(z)}{z} = 100/\gamma_0 \approx 10(R_0/L) \approx 0.01, \tag{37}$$

giving Θ in radians. Here we combine Equations (39) and (53) in Colgate et al. (2015), giving $\gamma_0 \approx 10(L/R_0) \approx 10^4$ as the average Lorentz factor of ions wandering in and out of the kink accelerator zone concentrated in the Central Column. An ion with $\gamma_0 \approx 10^4$ for the most extreme field line excursions is to be compared with a maximum of order 10^7 in Equation 11(b).

5.5. Possible Signatures from Escaping Cosmic Rays Beyond Lobes

We call attention to a potential source of strong radiation beyond the jet/lobe regions. Two-stream interaction of ambient electrons and cosmic-ray ions recycling through this region would heat ambient electrons to energies comparable to cosmic-ray energies. This electron heating would give rise to synchrotron radiation in the weak magnetic field beyond the jet/lobe regions. Together with radiolobe radiation, this ambient synchrotron radiation ahead of the nose can also produce IC radiation in the ambient, which could pair cascade and so on. This two-stream effect obeys the same relativistic equations giving two-stream in the jet, as discussed in Appendix B.2.

6. Transient versus Quasi-static Acceleration

Both transient acceleration (e.g., magnetic reconnection, shocks) and our quasi-static model can be described by the electric field $\mathcal{D}$ (hyper-resistivity) in Equation (2). One difference is whether electric fluctuations $\boldsymbol{E}_1$ yielding $\mathcal{D}$ are electrostatic in our reference frame (as in our model; e.g., Equation 13(b)), or inductive (reconnection). The other difference is whether particle acceleration is parallel to $\boldsymbol{B}$ (as in the jet, Section 3.2) or perpendicular (as in the nose, Section 3.3). Perpendicular acceleration (ions or electrons) is described by $d(\mu B)/dt$ (magnetic moment μ). Fermi acceleration is $\partial B/\partial t$ at constant μ (inductive); DCLC is $d\mu/dt$ at constant B (requiring cyclotron resonance).

An important result from our model is that cosmic-ray acceleration occurs, not in giant radiolobes, but rather from the jet nose. We refer the readers to the discussion around Equation (8), which can be summarized as follows. Near the disk and jets within the pc-scale, strong kink modes and transient reconnection could explain phenomena such as gamma-ray flares. But overall, jet kink modes driven by the disk become self-stabilizing, growing weaker along the jet. The net result is that the total voltage drop due to kinks is only

$0.01\mathcal{V}$, in Equation (9), consistent with overall jet luminosity (Krolik 1999). Weak electron heating giving the observed electromagnetic radiation occurs mainly in the magnetically collimated jet, which serves as a (flexible) conduit of power from the disk to the nose. A different argument follows from considerations of the free energy δW in kink modes, mentioned in Section 5.1. Let us compare δW for internal kinks giving $\Delta \mathcal{V}$ above with that for external kinks needed to fill radiolobes, giving $\delta W \propto k_z^2 \xi_a^2$ (with line displacement ξ_a; Colgate et al. 2015, Equations (22) and (24)). That $\delta W_{\mathrm{external}} \ll \delta W_{\mathrm{internal}}$ follows from $k_z a \approx 1$ for internal modes versus $k_z a \ll 1$ for external modes. That $\delta W_{\mathrm{internal}}$ gives weak current diffusion into radiolobes was discussed in Colgate et al. (2015).

While our model places the majority of cosmic-ray acceleration by jets in their nose region, this does not preclude intense flaring events excited possibly by kink instabilities as well as reconnection within the jet itself, leading to flares (e.g., Giannios et al. 2009; Zhang et al. 2017; de Gouveia Dal Pino et al. 2019). Further studies are needed to examine the relationship between these processes.

That UHECR's are mainly produced in the nose is a version of magnetic-to-kinetic conversion at the nose-end of propagating jets. To compete with quasi-static DCLC cosmic-ray power, the magnetic energy in the nose must be dumped in a time $<0.01\tau$. While this could not be sustained, transient energy conversion by reconnection might account for the small flux in UHECRs at energies $>10^{20}$ eV (dynamo voltage; Fowler et al. 2009a).

7. Summary of Results

In this fourth paper of our series of papers on UHE cosmic-ray acceleration mentioned in the introduction, we have shown that the jet model developed in Colgate et al. (2014, 2015) automatically leads to a quasi-static accelerator as an alternative to transient models invoking acceleration by shocks and magnetic reconnection. Besides theoretical arguments in the introduction, evidence for the model includes order-of-magnitude predictions listed in Table 2, with references to the text. The jet input parameters, listed in Table 1, are determined by the conservation of energy and angular momentum, valid within our model approximating the jet boundary as a rectangle, justified in Colgate et al. (2015). Predictions such as 1% of jet power in electromagnetic radiation involve estimates of turbulence transport rates. Where possible, we take advantage of cancellations of turbulence diffusion coefficients so that exact magnitudes are not required, an example being our derivation of the $1/E^3$ scaling law for the UHE cosmic-ray intensity.

As noted in the introduction, it is our hope that our model will stimulate interest in computer simulations of jet evolution and particle acceleration designed to include effects of kinetic-driven turbulence involving both electrons and ions. Since many timescales are involved, different codes emphasizing different phenomena will still be required, with guidance from our model how to separate phenomena. A test of our model that could be applied to existing GRMHD codes would be a diagnostic like that in Figure 4, yielding evidence that jets will become magnetically collimated on timescales short compared to jet lifetimes but long compared to GRMHD run times.

Perhaps our most surprising prediction is strong recycling of ions between the jet nose and the ambient shock ahead of the nose, in Section 4.4. Recycling plays an essential role in our calculation of UHE intensity on Earth, in Section 4.3. We draw attention to an as yet unexplored signature of recycling, mentioned in Section 5.5. This concerns radiation due to heating of ambient electrons in front of the jet nose, in the region of strong recycling of cosmic-ray ions. Two-stream interaction between escaping cosmic-ray ions and ambient electrons could heat electrons to cosmic-ray energies.

Appendix A
Short-circuit in the Disk: Why GRMHD Simulations Should Evolve Toward a Magnetically Collimated Jet

We describe the launching of jets by the following equations:

$$\boldsymbol{E} + \frac{1}{c}\boldsymbol{v}_\perp \times \boldsymbol{B} = -\frac{1}{c}\frac{\partial \boldsymbol{A}}{\partial t} - \nabla\Phi + \frac{1}{c}\boldsymbol{v}_\perp \times \boldsymbol{B} = \mathcal{D}, \quad (38a)$$

$$\frac{d\boldsymbol{P}}{dt} = \frac{\partial \boldsymbol{P}}{\partial t} + \nabla \cdot \sum \int dp f\left(\frac{\boldsymbol{pp}}{m\gamma_{\mathrm{L}}}\right)$$
$$= \frac{1}{c}\boldsymbol{j} \times \boldsymbol{B} + \sigma\boldsymbol{E} = \frac{1}{c}\boldsymbol{j}_\perp^* \times \boldsymbol{B}, \quad (38b)$$

$$\sigma = \frac{\nabla \cdot \boldsymbol{E}}{4\pi}, \quad (38c)$$

$$\boldsymbol{j}_\perp^* \equiv \boldsymbol{j}_\perp - \sigma c\left(\boldsymbol{E} \times \frac{\boldsymbol{B}}{B^2}\right) = -\frac{c}{B^2}\left(\frac{d\boldsymbol{P}}{dt} \times \boldsymbol{B}\right), \quad (38d)$$

$$\left(\frac{1}{c}\boldsymbol{j} \times \boldsymbol{B} + \sigma\boldsymbol{E}\right)_r = \frac{1}{c}j_\phi B_z - \frac{1}{8\pi r^2}\frac{\partial}{\partial r}r^2(B_\phi^2 - E_r^2) = 0. \quad (38e)$$

Equation 38(a) is Ohm's law in Equation (2), with fluid velocity $\boldsymbol{v}$, vector potential $\boldsymbol{A}$, electrostatic potential Φ and hyper-resistivity $\mathcal{D}$ representing any kind of turbulence, MHD or kinetic (Fowler & Gatto 2007). Equation 38(b) is the momentum equation, with $\gamma_{\mathrm{L}} = \left[1 + \left(\frac{p}{mc}\right)^2\right]^{1/2}$, and it includes the electric force due to space charge density σ, given in Equation 38(c). To obtain Equation 38(d), in Equation 38(b) we take the cross-product with $\boldsymbol{B}$ from the right, giving $\frac{d\boldsymbol{P}}{dt} \times \boldsymbol{B}$ and on the far-right-hand side $-c^{-1}\boldsymbol{j}_\perp^*$. Equation 38(d) is the solution to Equation 38(b), giving $\boldsymbol{j}_\perp^*$ as acceleration-driven
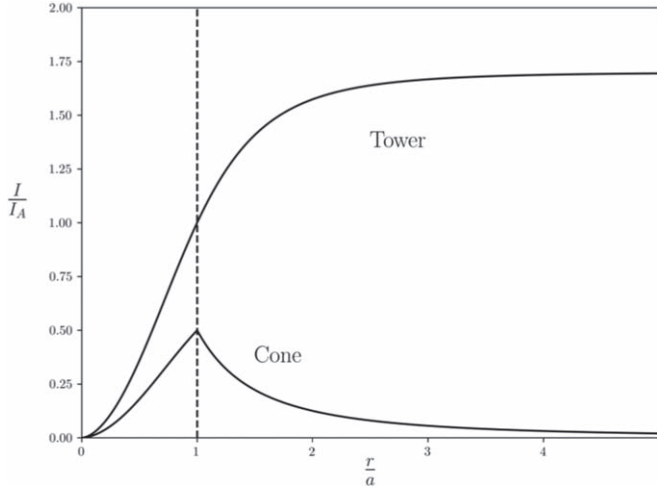
Figure 3. Threshold current $I(r) = rB_\phi c/2$ profile for onset of a conical jet (bottom curve) and a magnetic tower jet (upper curve, from Paper I).

current flow between flux surfaces moving at velocity $v_\perp = c(E \times B/B^2)$ in our reference frame.

Equation 38(e) is the Force Free Degenerate Electrodynamics model assuming $\mathcal{D} = 0$ (Meier 2012). This equation describes one-dimensional jet equilibria near the black hole. It has the two solutions shown in Figure 3, distinguished by the magnitude of B_ϕ compared to E_r due to disk rotation. We imagine accretion around a pre-existing black hole threaded by pre-existing poloidal (r, z) magnetic flux with current j initially zero in the neighborhood of the black hole. As MRI turns on, E_r due to rotation drives j_z giving B_ϕ, which grows until a jet is launched when $B_\phi = E_r$ and $j_\phi = 0$. This jet is uncollimated, corresponding to the curve labeled "cone" in Figure 3. If the jet current could continue to grow, finally a collimated jet with $j \times B = 0$ ($B_\phi \gg E_r$) would emerge, described by the upper curve labeled magnetic "tower" in Figure 3 (Lynden-Bell 1996, 2003, 2006; Li et al. 2006).

That the accretion disk current does continue to grow sufficiently to launch a magnetic tower can be seen as follows. The growth of the disk current in terms of the vector potential A is described by Equation 38(a) with $\mathcal{D}$ equal to that for MRI. Near the black hole, the growth rate ($|c\mathcal{D}/A|$) will turn out to be of the order of the accretion rate (v_r/a), giving a rapid buildup of dynamo current to balance gravitational energy input by accretion (this process takes only years, accessible by GRMHD simulations). We obtain inside the disk:

$$\frac{\partial A_r}{\partial t} - \left(v_\phi B_z - c\frac{\partial \Phi}{\partial r} \right) \approx \frac{\partial A_r}{\partial t} \approx -(v_z B_\phi + c\mathcal{D}_r), \quad (39a)$$

$$\frac{\partial A_\phi}{\partial t} = -(v_r B_z - v_z B_r + c\mathcal{D}_\phi), \quad (39b)$$

$$c\frac{\partial \Phi}{\partial r} = v_\phi B_z, \quad (39c)$$

$$\frac{E_r}{B_\phi} \approx \left(-\frac{\partial \Phi}{\partial r} \right)/B_\phi = -\frac{v_\phi}{c}\left(\frac{B_z}{B_\phi} \right) = \frac{v_\phi}{c}\left(-\frac{\mathcal{D}_\phi}{\mathcal{D}_r} \right)\left(\frac{v_z}{v_r} \right) \ll 1, \quad (39d)$$

$$-\frac{\mathcal{D}_\phi}{\mathcal{D}_r} \approx 1, \quad (39e)$$

$$-\left(\frac{\mathcal{D}_\phi}{\mathcal{D}_r} \right)_{\mathrm{MRI}} = \left| \frac{\langle v_1 \times B_1 \rangle_\phi}{\langle v_1 \times B_1 \rangle_r} \right| \approx (\gamma_{\mathrm{MRI}}/\Omega) \leqslant 1. \quad (39f)$$

We note that, as the disk develops MRI, these equations show that $B_\phi \approx \partial A_r/\partial z$ gradually grows from zero, until reaching $B_\phi = E_r$, which launches the conical jet, but then continuing smoothly to the value needed to sustain a magnetic tower. This gradual growth of B_ϕ inside the disk, independent of the jet, leads us to postulate the creation of a short-circuit in the corona isolating the growing current in the disk from a constant current in the jet. Though initially $B_\phi < E_r$, it grows smoothly to equal and surpass E_r, discussed as follows.

In Equations 40(a) and (b), we apply Equation 39(c) to eliminate zeroth-order terms, leaving $\frac{\partial A}{\partial t} \approx -c\mathcal{D}_{\mathrm{MRI}}$ as the driver of the self-excited dynamo magnetic field. Then Equation 39(d) gives the steady state with $E_r \ll B_\phi$ obtained as follows. We set $\partial A_r/\partial t = \partial A_\phi/\partial t = 0$ and drop $v_z B_r$ compared to $v_r B_z$ inside the disk, giving then $B_\phi = -(c\mathcal{D}_r/v_z)$ and $B_z \approx -(c\mathcal{D}_\phi/v_r)$ in quasi-steady state. Most importantly, we apply Equation 39(e), derived for an ordering $|v_r/v_\phi| \ll 1$ in Colgate et al. (2014), and consistent also with MRI theory, by Equation 39(f) using (correlated) perturbations v_1 and B_1 and growth rate $\gamma_{\mathrm{MRI}} \leqslant 0.75\Omega$ in Balbus & Hawley (1998), Section IV.B.

Equation 39(d) shows why B_ϕ in the disk grows to exceed E_r in the disk, enough so to drive the jet current $I(r)$ up to the magnetic tower threshold in Figure 4.

Why a magnetic tower does not form immediately concerns the persistence of the initial conical jet. This is due to the jet structure whereby the jet current returns close to the outgoing jet so that jet magnetic energy only changes as the length L changes, at a rate $\frac{dL}{dt} = c$ (Appendix C, Colgate et al. 2015; Blandford & Anantua 2017). The only way that the disk current can continue to grow, while the jet persists at the lower current associated with the conical jet in Figure 3, is that a short-circuit develops in the disk corona. The required short-circuit is automatically accommodated by $j_\perp^*$ in Equation 38(d). This occurs through the kinetic term of $d\mathbf{P}/dt$ that allows a quasi-steady ($\partial \mathbf{P}/\partial t = \mathbf{0}$) conical jet to persist even as the disk current continues to grow, giving then the short-circuit current $I_\perp$ and a corresponding parallel current $I_\parallel$ as follows:

$$I_\perp = 2\pi r \Delta_z j_{\perp r}^* = \left(\frac{crB_\phi}{2} \right)_{r=a} \sum \int d\mathbf{p}\, f\left(\frac{4\pi p_{\perp z}^2}{m\gamma_L B_\phi^2} \right)$$
$$\approx \frac{1}{2}I\left(\frac{v_{\perp z}}{v_A^*} \right)^2, \quad (40a)$$

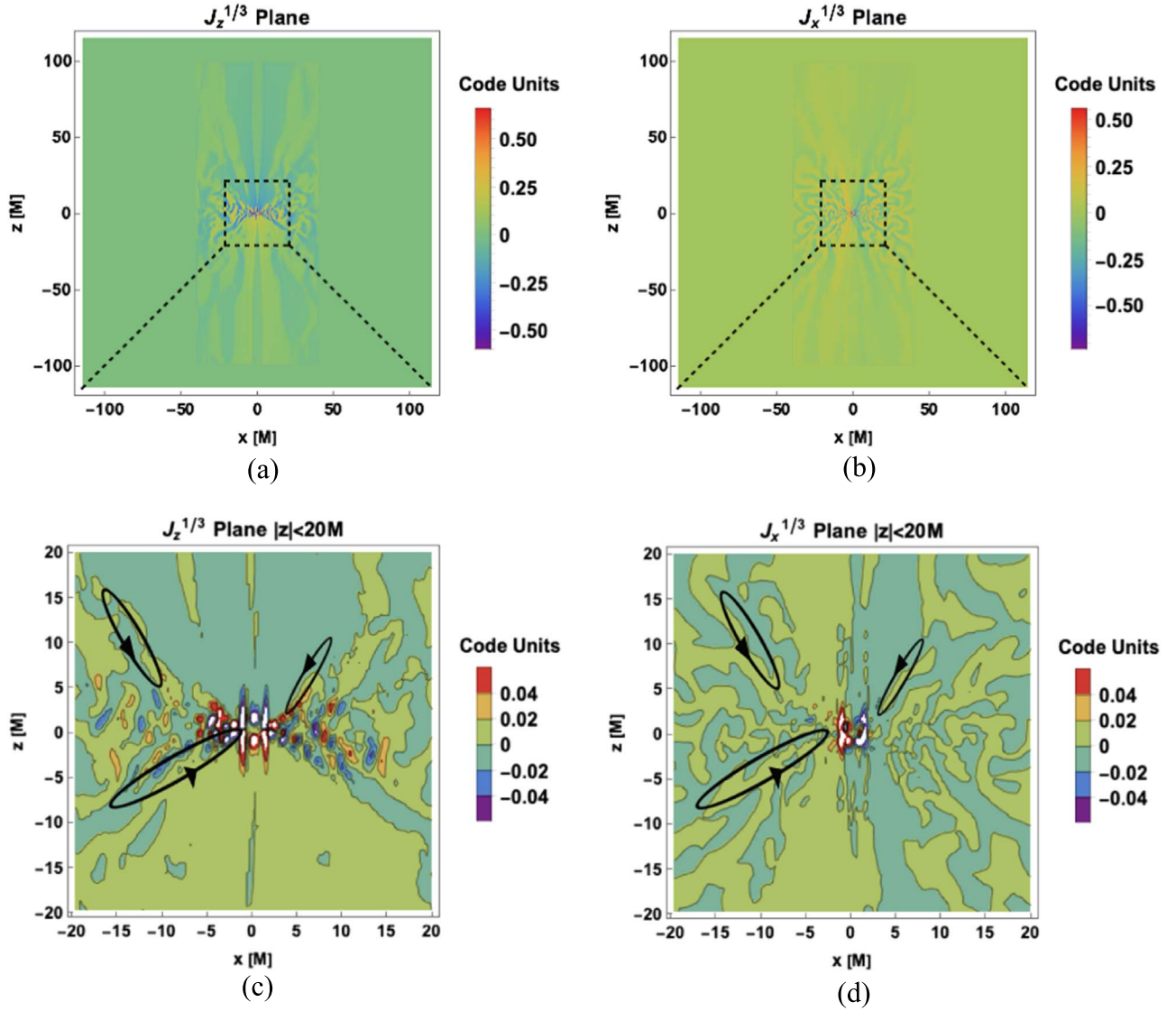$$I_\parallel = I - 2I_\perp = I\left(1 - \frac{v_{\perp z}^2}{v_A^{*2}} \right), \quad (40b)$$

$$E_r = \frac{1}{c}(r\Omega|B_z| + v_z B_\phi), \quad (40c)$$

$$v_A^* \approx c\left[\frac{B_\phi}{\sqrt{B_\phi^2 + 4\pi nmc^2}} \right], \quad (40d)$$

$$I(\mathrm{disk}) = I_\parallel + I_\perp(\mathrm{corona}) + I_\perp(\mathrm{nose}). \quad (40e)$$

Here Δ_z is the width of the current path and the factor $\left(\frac{crB_\phi}{2} \right)_{r=a} = I$ is the final disk current with factor $\frac{1}{2}$ fitted to

Figure 4. As discussed in the text, this figure shows evidence for a short-circuit current in the disk/coronal region of GRMHD simulations (McKinney et al. 2012). Panel (a) shows the vertical z-component of conical jet currents emerging up and down from the accretion disk and returning in a close-fitting jacket surrounding the jet (note J_z goes down in the dark green regions and up in light green regions); the inner $-20M < x, z < 20M$ region is expanded as follows, where $M = 0.5R_S$ (Schwarzschild radius). Panel (c) expands the region in Panel (a) closest to black hole, with overlaid drawings following possible looping paths of short-circuit currents. Panel (b) shows MRI-driven 3D activity in the radial component of the current; the inner $-20M < x, z < 20M$ region is expanded as follows in Panel (d) (note J_x goes left in the dark green regions and right in light green regions).

Figure 4 at $r = a$. Equation 40(a) is obtained from Equation 38(d) with $\frac{dP}{dt}$ from Equation 38(b) with $\frac{\partial P}{\partial t} = 0$. The cross-product of $\left(\frac{dP}{dt} - \frac{\partial P}{\partial t}\right)$ with $\boldsymbol{B}$ gives $p_{\perp z}B_\phi$; and maximizing on the divergence gives $\Delta_z(\nabla \cdot \boldsymbol{p}) = p_{\perp z} = m\gamma_L u_{\perp z}$. The final expression approximates the integral over $u_{\perp z}$ by the fluid velocity $v_{\perp z}$ divided by the Alfvén-like velocity v_A^* in Equation 40(d). Equation 40(c) is Ohm's law in the conical jet, whereby jet acceleration to $v_{\perp z} \approx c$ maintains $E_r = B_\phi$ in the jet.

The distinction between $I_\perp$ and $I_\parallel$ in Equations 40(a) and (b) reflects a branching of the total dynamo current, with up to three distinct branches summed up to give the total dynamo current in Equation 40(e). While the MRI-driven current for a magnetic tower must close along closed poloidal field lines (as in Figure 1), the current loop of the initial conical jet closes via a current $I_\perp$ flowing directly across poloidal flux surfaces. This

$I_\perp$ flows across the nose of the growing jet. But because the conical jet current remains constant as the disk current continues to increase, a short-circuiting $I_\perp$ must also flow in the corona, giving the disk current as the sum of three branches in Equation 40(e). We take the conical jet current equal to its return current at the nose so that Equation 40(e) gives $I_\parallel = I - 2I_\perp$ in Equation 40(b).

The transition from cone to tower is driven by anything slowing down the jet, giving, by Equation 40(a), $I_\perp \to 0$ as $v_{\perp z} = dL/dt \to 0$. The slowing down of jets can be described by an electric circuit satisfying energy conservation Colgate et al. (2015). We obtain:

$$\frac{\partial}{\partial t}\left[\frac{B^2 + E^2}{8\pi}\right] + \boldsymbol{v} \cdot \frac{d\boldsymbol{P}}{dt} + \nabla \cdot \left(\frac{c\boldsymbol{E} \times \boldsymbol{B}}{4\pi}\right) = -\boldsymbol{v} \cdot \rho\nabla V_G,$$

(41a)

$$f_{\text{dis}}(I\mathcal{V}) = \frac{d}{dt} \int dx \left(\frac{B^2 + E^2}{8\pi} \right)$$

$$\approx \frac{d}{dt} \left\{ L \left(\frac{I}{c} \right)^2 \left[1 + \frac{I_\perp^2}{I^2} \ln \left(\frac{R_2(z)}{R_1(z)} \right) \right. \right.$$

$$\left. \left. + \frac{I_\parallel^2}{I^2} \ln \left(\frac{R}{a} \right) \right] \right\}, \qquad (41b)$$

$$\frac{dL}{dt} \approx \frac{f_{\text{dis}}\, c}{1 + \frac{1}{4} \frac{v_{\perp z}^4}{v_A^{*4}} \ln \left(\frac{R_2(z)}{R_1(z)} \right) + \left(1 - \frac{v_{\perp z}^2}{v_A^{*2}} \right)^2 \ln \left(\frac{R}{a} \right)}, \qquad (41c)$$

$$\frac{dL}{dt} \rightarrow \frac{f_{\text{dis}}\, c}{1 + \ln \left(\frac{R}{a} \right)}; \quad v_{\perp z} \ll v_A^*, \qquad (41d)$$

$$f_{\text{dis}} = \frac{1}{2}(1 - f_{\text{conv}}). \qquad (41e)$$

Equation 41(a) is obtained in the usual way by adding the results from dotting $\boldsymbol{v}$ into Equation 38(b) and dotting $\boldsymbol{B}$ into Maxwell's $\frac{\partial \boldsymbol{B}}{\partial t}$ equation, using Equation 38(a) giving $\boldsymbol{v} \cdot \boldsymbol{E} = 0$ if we neglect $\mathcal{D}$ in the jet. Integrating Equation 41(a) over the jet volume gives Equation 41(b), with dynamo power on the left-hand side (from the Poynting vector in Equation 41(a)), and in Equation 41(e) a dissipation factor f_{dis} with f_{conv} as the efficiency of converting magnetic energy to ion acceleration and a factor $1/2$ representing ambient shocks, as in Colgate et al. (2015). Equation 41(b) approximates the jet as a conical jet with current $I_\perp$ bounded by $R_1(z) < r < R_2(z)$ and embedded inside a magnetic tower with current $I_\parallel$ bounded by $a < r < R$. We drop E and divide $\int dx B^2$ into three parts: (a) the Central Column giving 1 in the bracket []; (b) the conical jet giving the term $\propto I_\perp^2$; and (c) the enveloping magnetic tower gives the term $\propto I_\parallel^2$, valid when $j_\parallel > j_\perp$, causing current to twist around field lines. As in sub-Alfvénic jets in spheromaks (Figure 2 Colgate et al. 2015), we use the fact that, as dL/dt falls below c, Alfvén waves at speed c (for the jet density in Table 1) spread flux radially to produce a blunt nose as shown in Colgate et al. (2015), whereby the jet can be approximated as a cylinder of fixed radius and expanding length L approximately independent of r so that L can be removed from the integral to give Equation 41(c).

Equation 41(c) derives the jet velocity $\frac{dL}{dt}$ from Equation 41(b) in quasi-steady state (constant I), using Equation 40(a) for $I_\perp$ and Equation 40(b) for $I_\parallel$. The slow growth of the jet current to match the final dynamo current is approximated by $c\mathcal{V}/I = 1$ giving the correct limits both as the jet slows down and when the jet is first launched with jet current $I = \mathcal{V}/Z_o = c\mathcal{V}$ (free space impedance, equivalent to $B_\phi = E_r$). The largely empty jet volume yields the characteristic logarithmic behavior already invoked in Equation (1), both for the final collimated magnetic tower with dimensions R and L, and the intermediate conical jet with inner radius $R_1(z)$ and outer radius $R_2(z)$.

A.1. GRMHD Simulations

Attempts to simulate the entire astrophysical jet formation cycle are limited by the extreme range of time and space scales, from accretion disk dynamos concentrated near the black hole, where conical jets are created, to the Mpc dimensions of fully developed jets. In particular, GRMHD codes yielding MRI-driven dynamos producing conical jets in a low density ambient do not yet exhibit the slowing down required to produce a tower (A. Tchekhovskoy 2017, private communication). That this is perhaps understandable given the limited timescale of these simulations follows from Equation 41(c) dropping $\ln(R/a)$ to obtain, for zero dissipation $(f_{\text{dis}} = 1)$, $dL/dt \approx c / \left[1 + \frac{1}{4} \ln(R_2/R_1) \right] > 0.8c$ for typical cone-dimensions in GRMHD simulations. On the other hand, assuming continued inductive slowing down of the jet as dissipation develops, eventually giving $f_{\text{dis}} = 1/4$ in Section 4.2, $I_\parallel = (15/16)I$ yielding $dL/dt \approx cf_{\text{dis}}/[1 + 0.9\ln(R/a)]$ as in Equation 41(d). Equation 41(d) predicts early slow-down to $dL/dt \approx 0.01c$ at 1% of the final jet length if we approximate $R(t) = 0.1L(t)$ in Equation 41(d), indicating magnetic collimation over most of the life of the jet.

The slowing down by $\ln R/a$ that produces a magnetically collimated tower is consistent with MHD simulations of magnetically dominated jets, relativistic in Guan et al. (2014), non-relativistic in Nakamura et al. (2006), Carey (2009), and Carey et al. (2011). Disk-like creation of jets by rotation of a conducting sphere in a dense ambient is featured in relativistic MHD simulations in Bromberg & Tchekhovskoy (2016), exhibiting jet slowing down by the ambient and the two classes of MHD kink modes used in our accelerator model (Nakamura et al. 2006, 2007; Tchekhovskoy & Bromberg 2016).

Future work might disclose other connections to our model, for example, the short-circuit current in Equation 40(a), as would be needed if the disk current continues to rise while the jet current remains constant (Equations 39(a)–(f)). We have examined GRMHD simulations in McKinney et al. (2012). We were unable with data available to us to show directly that the disk current does continue to rise at constant jet current. We did, however, find the evidence in Figure 4 that could be interpreted as short-circuiting current loops. Shown are trajectories of $j^{1/3}$ (to add contrast) in Cartesian x–z planes cutting through 3D current structures ($|x|$ being r at $y = 0$). The predicted short-circuiting current loops are indicated by overlays in Panels (c) and (d), occurring within a radius $r = a = 20M \equiv 10R_S$, this being the zone of greatest gravity-driven MRI activity as calculated in Section 2. The tilting geometry of actual loops gives evidence of looping both in j_z in Panel (c) and in j_x in Panel (d). Note that the disk/corona region is likely to be highly turbulent where magnetic reconnection is expected (e.g., Ball et al. 2018; Kadowaki et al. 2018), though such reconnection processes should not preclude the short-circuit paths to exist.

Appendix B
Relativistic DCLC and Two-stream Instability

In this appendix, we review the relativistic derivation of Equation (14) giving, with all terms included, two-stream instability in the Central Column, and also DCLC instability in the nose that account for UHECR acceleration in our model. Both two-stream and DCLC dispersion relations used in this paper appear in the past literature. These are electrostatic modes with perturbation Φ_1. Here we only sketch the derivations that relate relativistic plasmas to well-documented non-relativistic plasmas in the laboratory.

The main features emerge in the "slab" (Cartesian) coordinate approximation, given by

$$\Phi_1(\boldsymbol{x},\,t) = \Phi_1(x)\exp\{i(k_z z + k_y y - \omega t)\}, \tag{42}$$

where z is the direction along $\boldsymbol{B}$, while y lies in the flux surface, and x is perpendicular to a flux surface (the direction of density gradients giving drift modes for DCLC). We write the unperturbed distribution function F_0 as $F_0(P_z, P_y, E_\perp) = n_0 f_0$, where $P_z = p_z$, $P_y = p_y + (q/c)A_y$ with charge q and $E_\perp = 1/2 p_\perp v_\perp$ with $p_\perp^2 = p_x^2 + p_y^2$. Here P_z, $E_\perp$ and the total energy $mc^2\gamma_L$ are relativistic constants of the motion in a uniform magnetic field. The mean-field density n_0 is defined by the normalization $\int dP_z\, dE_\perp\, dP_y f_0 = 1$, and similarly the perturbation $F_1 = n_0 f_1$. Solving the linearized Vlasov equation for f_1 and integrating F_1 to get the density perturbation, we obtain

$$n_1 = n_0 \int dP_z\, dE_\perp\, f_1, \tag{43a}$$

$$= n_0 \int dP_z\, dE_\perp \int_{-\infty}^{t} dt'\, iq\Phi_1\left(k_y \frac{\partial f_0}{\partial E_\perp} v'_y + k_z \frac{\partial f_0}{\partial P_z}\right)$$
$$\times \exp\{i[k_y(y'-y) + k_z(z'-z) - \omega(t'-t)]\}, \tag{43b}$$

$$= n_0 q\Phi_1 \int dP_z\, dE_\perp$$
$$\times \left\{ \frac{\partial f_0}{\partial E_\perp}\left(1 - \sum\left[\frac{\omega - k_z v_z}{\omega - k_z v_z - n\omega_c} J_n(k_y r_L)^2\right]\right) \right.$$
$$\left. - \sum k_z \frac{\partial f_0}{\partial P_z}\left(\frac{1}{\omega - k_z v_z - n\omega_c}\right) J_n(k_y r_L)^2 \right\}. \tag{43c}$$

Adding dependence on $P_y = p_y - (e/c)A_y$ gives electron drift waves, yielding an additional term of the form

$$\frac{\partial(n_0 f_{e0})}{\partial P_y} = n_0\left(\frac{1}{\partial P_y/\partial p_y}\right)(\partial f_{e0}/\partial P_y)$$
$$+ f_{e0}\left(\frac{1}{\partial P_y/\partial x}\right)(\partial n_0 f_{e0}/\partial x)$$
$$= n_0\left(\frac{\partial f_{e0}}{\partial P_y} + f_{e0}\frac{\varepsilon c}{qB}\right), \tag{44}$$

where $\varepsilon = (\partial n_0/\partial x)/n_0$. Integrating first over the orbit and then over momentum gives the drift contribution to the density perturbation. We obtain for the charge density

$$q(n_1)_{\text{drift}} = \Phi_1 n_0 e^2 k_y\left(\frac{\varepsilon c}{qB}\right)\sum \frac{J_n(k_y r_L)^2}{\omega - k_z v_z - n\omega_c}, \tag{45a}$$

$$\rightarrow \Phi_1 n_0 e^2 k_y\left(\frac{\varepsilon c}{qB\omega}\right) = \frac{\Phi_1 k_y \varepsilon}{4\pi}\left(\frac{\omega_{pe}^2}{\omega_{ce}\,\omega}\right). \tag{45b}$$

Growth of v_y or a pre-existing v_y adds ion cyclotron resonance terms to the left-hand side of Equation (14). Resonance gives large contributions from the ion Bessel functions in Equation 43(c), but only if $k_y r = 1$ inside the plasma. That this cannot happen in the Central Column follows

from

$$k_y a = \varepsilon a\left(\frac{\omega_{pe0}^2}{\omega_{ce0}\omega_{ci0}}\right)\gamma_{\text{CC}} = 4.4 \times 10^{-4} M_8 \ll 1, \tag{46}$$

where the subscript 0 denotes rest mass quantities. We see that $k_y a = 1$ is not possible for any known black hole mass. In laboratory experiments, these ion cyclotron modes occurred when the non-relativistic $\Omega_{ci} < \omega_{pi}$ (Post 1981) or, equivalently, when

$$\left(\frac{\omega_{pi}}{\Omega_{ci}}\right)^2 = \beta_{i\perp}\left(\frac{c}{v_\perp}\right)^2 > 1. \tag{47}$$

Equation (47) is an approximate condition for DCLC instability with pressure parameter $\beta_{i\perp}$ in Equation 17(c). This can be satisfied in the laboratory at low $\beta_{i\perp}$ if $v_\perp \ll c$, but in AGN jets it is satisfied only as ions enter the nose.

B.1. Relativistic DCLC

A DCLC dispersion relation like the non-relativistic form giving the DCLC instability threshold in Equation 15(c) can be derived from Equation 43(c) applied to ions. The non-relativistic derivation, in Post & Rosenbluth (1966) reproduced in Fowler (1981), follows the same steps that led to Equation 43(c). Relativity would appear only in the mass defining the cyclotron frequency. The result, using also the drift term discussed previously, is given by

$$k_y^2 = k_y \varepsilon\left(\frac{\omega_{pe0}^2}{\omega_{ce0}\,\omega}\right), \tag{48a}$$

$$- \omega_{pi0}^2 \int dP_z\, dE_\perp\left\{ m_i \frac{\partial f_0}{\partial E_\perp}\left[1 - \sum J_n(k_y r_{Li})^2 \frac{\omega}{\omega - n\Omega_{ci}}\right]\right\}. \tag{48b}$$

Instability requires $\frac{\partial f_0}{\partial E_\perp} > 0$ near $E_\perp = 0$, representing the "hole" in perpendicular energy discussed in Section 3.3.2. It was found that, mathematically, a sufficient hole is present when the large Larmor orbits cause the P_z-averaged distribution $\int dP_z\, dE_\perp\, \frac{\partial f_0}{\partial E_\perp}$ to be strongly positive while a Maxwellian in $E_\perp$ would give a negative value. Given a hole, Equations 48(a), (b) is identical with the non-relativistic formulation, aside from swapping P_z for v_z in the integration, giving relativistic masses but otherwise identical with the DCLC instability in non-relativistic form with relativistic masses, as in Equation 23(a).

B.2. Two-stream Instability

To obtain the dispersion relation giving two-stream instability between counter-streaming ions and electrons in the Central Column, we set $\varepsilon = 0$ in Equation (44) giving n_1 by Equation 43(c) with $k_y = 0$, and we take the limit $k_y r_L \rightarrow 0$ in all Bessel functions giving $J_o \rightarrow 1$ and $J_n \rightarrow 0$ for all $n \neq 0$. We assume ions are accelerated to velocity $v_z = c$ and electrons to velocity $v_z = -c$. Poisson's equation becomes

$$k_z^2\Phi_1 = -4\pi n_0 e^2\Phi_1 k_z \int dP_z\, dE_\perp \sum_{j=e,i} \frac{\partial f_{0j}}{\partial P_z}(\omega - k_z v_z)^{-1}, \tag{49a}$$

$$1 = \left(\frac{\omega_{pe0}^2}{\gamma_{\rm Le}^3}\right) f_{e0} \frac{1}{(\omega + k_z c)^2} + \left(\frac{\omega_{pi0}^2}{\gamma_{\rm Li}^3}\right) f_{0i} \frac{1}{(\omega - k_z c)^2}. \quad (49b)$$

In Equation 49(a), setting $k_y = n = 0$ has eliminated terms with $\frac{\partial f_0}{\partial E}$ giving n_1 in Equation 43(c). Equation 49(b) follows on dividing by $k_z^2 \Phi_1$ after applying the following result in Montgomery & Tidman (1964), Equations (10.51) and (10.52). Using $P_z = p_z$ and $\gamma_{\rm L}$ with relativistic $v_z = (p_z/m\gamma_{\rm L})$, we obtain

$$m\frac{\partial v_z}{\partial p_z} = \frac{1}{\gamma_{\rm L}^3}[\gamma_{\rm L}^2 - (p_z^2/m^2 c^2)]$$
$$= \frac{1}{\gamma_{\rm L}^3}[1 + (p_\perp^2/m^2 c^2)] \approx \frac{1}{\gamma_{\rm L}^3}. \quad (50)$$

We note that the ion term in Equation 49(b) is largest at resonance, suggesting that we take $\omega = k_z c + \Delta\omega$ near the ion resonance (Goldston & Rutherford 1995, Section 23.4). Upon substituting $\omega = k_z c + \Delta\omega$ and expanding, Equation 49(b) gives

$$k_z^2 = k_z^2\left[\frac{\omega_{pe}^{*2}}{(\omega + k_z c)^2} + \frac{\omega_{pi}^{*2}}{(\omega - k_z c)^2}\right], \quad (51a)$$

$$= k_z^2 \frac{\omega_{pe}^{*2}}{(2k_z c)^2}\left(1 - \frac{\Delta\omega}{k_z c} + ...\right) + \frac{\omega_{pi}^{*2}}{\Delta\omega^2}k_z^2, \quad (51b)$$

$$k_z c = \frac{1}{\sqrt{2}}\omega_{pe}^*, \quad (51c)$$

$$\Delta\omega^3 = (k_z c\, \omega_{pi}^{*2}) = (k_z c)^3\frac{\omega_{pi}^{*2}}{2\omega_{pe}^{*2}} = (k_z c)^3\frac{m_e}{2m_i}, \quad (51d)$$

$$\omega = k_z c + \Delta\omega = k_z c\left[1 + \left(\frac{m_e}{2m_i}\right)^{1/3}(\cos 60° + i\sin 60°)\right], \quad (51e)$$

where ω in Equation 51(e) is the unstable root. Here $\omega_p^{*2} = (4\pi n_0 e^2/m\gamma_{\rm L}^3)$. In the Central Column, radiation-limited acceleration gives $\gamma_{\rm Li} \gtrsim \gamma_{\rm Le}$ by Equation (18), including electron synchrotron radiation, giving then the ratio of rest masses in Equations 51(d) and (e) so that the only relativistic effect is the speed of light as the wave velocity.

Once initiated, the two-stream instability can scatter electrons to transfer parallel acceleration to synchrotron radiation, as in Section 5.1. To do so, the electron beam must excite waves with non-zero k_y, which adds terms to the dispersion relation in Equation 49(b). Keeping both the electron drift term from Equation (44) and potentially resonant ion terms with finite k_y, we obtain

$$k_y^2 + k_z^2 = \left\{\int dP_z\, dE_\perp f_{e0}\left[\frac{k_z^2}{\gamma_{\rm Le}^3}\frac{\omega_{pe0}^2}{(\omega - k_z v_z)^2}\right]\right.$$
$$\left. + k_y\varepsilon\frac{\omega_{pe0}^2}{\omega_{ce0}\omega}\right\}_{\rm wave}, \quad (52a)$$

$$+ \left\{L_{\rm L} + \left[k_z^2\frac{(\omega_{pi0}^2/\gamma_{\rm CC}^3)}{(\omega - k_z c)^2}\right]\right.$$
$$\left. + k_y^2\left[J_1(k_y r_{\rm Li})^2\frac{\omega_{pi0}^2}{(\omega - k_z c - \Omega_{ci})^2}\right]\right\}_{\rm drive}, \quad (52b)$$

$$L_{\rm L} = i\pi(\omega_{pe0}^2 m_e^2)\left\{\int dP_z\, dE_\perp\, \delta\left(P_z - \frac{m_e\gamma_{\rm Le}\omega}{k_z}\right)\gamma_{\rm Le}\frac{\partial f_{e0}}{\partial P_z}\right\}, \quad (52c)$$

$$\approx i\pi\left(\frac{\omega_{pe0}^2}{c^2}\right)\left[(m_e^2 c^2)\frac{\partial f_{e0}}{\partial P_z}\right]_{\rm res}. \quad (52d)$$

Terms labeled "wave" generate the waves driven unstable by the terms labeled "drive," with $\gamma_{\rm CC}$ from Equation 19(b). In the absence of scattering, f_{e0} becomes a delta-function giving the result in Equation 52(a). Ions do not scatter, as discussed in Section 3.2, giving in the drive term in Equation 52(b) the same ion term as that in Equation 51(b), together with a new term taking into account cyclotron resonance. This ion cyclotron term comes from Equation 43(c) but dropping the $n = 0$ term of order $k_y^2(k_y^2 r_{\rm Li}^2)$ compared to k_y^2 on the left-hand side of Equation 52(d).

Lastly, we include in the drive term an imaginary contribution $L_{\rm L}$ from the electron Landau pole, whereas the integral in Equation 52(a) is to be interpreted as the principal part. The factor $\gamma_{\rm Le}$ in the Landau term arises from changing variables from v_z to P_z. The Landau pole gives damping or inverse damping depending on signs. The magnitude of the Landau damping term in Equation 52(c), comparable to other electron terms and much larger than ion terms away from resonance, indicates that Landau damping would cause electron momentum diffusion to stop short of the ion resonance. Resonance extends between positive $1 > v_z/c > (1 - \Delta\omega/k_z)$, giving the following allowed spread of electron velocities with no Landau damping

$$1 > \frac{v_{ze}}{c} > \left(1 - \frac{\Delta\omega}{k_z}\right) = \left[1 - \left(\frac{m_e}{2m_i}\right)^{1/2}\cos 60°\right] = 0.99. \quad (53)$$

Thus, as noted in Section 3.2, a uniform spread in electron momentum gives negligible net velocity and negligible electron current while avoiding electron resonance giving Landau damping. That Landau damping exists but ceases if there are few resonant electrons has been demonstrated conclusively in laboratory experiments in the low density regime relevant to AGN jets (Post 1981). One can show the necessary condition that k_y (surrogate for k_r) fits inside the Central Column is satisfied.

Once initiated, the two-stream instability can scatter electrons to transfer parallel acceleration to synchrotron radiation, as in Section 5. In principle, scattering can be described by a quasi-linear transport equation analogous to Equation 21(a) for ions that led to $1/E^3$ scaling of comic ray intensity in Section 4. Given the electron energy distribution, synchrotron and inverse Compton radiation could be calculated, as in Li & Kusunose (2000).

ORCID iDs

Hui Li ● https://orcid.org/0000-0003-3556-6568

References

al-Karkhy, A., Browning, P. K., Cunningham, G., Gee, S. I., & Rusbridge, M. G. 1993, PhRvL, 70, 1814
Alves, E. P., Zrake, J., & Fiuza, F. 2018, PRL, 121, 245101
Balbus, S. A., & Hawley, J. F. 1998, RvMP, 70, 1
Baldwin, D. E. 1977, RvMP, 49, 317
Ball, D., Özel, F., Psaltis, D., Chan, C.-K., & Sironi, L. 2018, ApJ, 853, 184
Begelman, M. C. 1998, ApJ, 493, 291
Begelman, M. C., Blandford, R. D., & Rees, M. J. 1984, RvMP, 56, 255
Berk, H. L., & Stewart, J. J. 1977, PhFl, 20, 1080
Beskin, V. S. 2010, PhyU, 53, 1199
Bierman, P. 1997, JPhG, 23, 1
Blandford, R., & Anantua, R. 2017, JPhCS, 840, 012023
Blandford, R., Meier, D., & Redhead, A. 2019, arXiv:1812.06025v1
Blandford, R. D. 1976, MNRAS, 176, 465
Blandford, R. D., & Payne, D. G. 1982, MNRAS, 199, 883
Blandford, R. D., & Znajek, R. L. 1977, MNRAS, 179, 433
Bromberg, O., & Tchekhovskoy, A. 2016, ApJ, 456, 1739
Carey, C. S. 2009, A Numerical Study of Magnetohydrodynamic Jet Collimation and Stability, PhD Dissertation, Univ. Wisconsin-Madison
Carey, C. S., Sovinec, C. R., & Heinz, S. 2011, University of Wisconsin Rep., www.cptc.wisc.edu/reports UW-CPTC 11-8.pdf (unpublished)
Colgate, S. A., Fowler, T. K., Li, H., et al. 2015, ApJ, 813, 136
Colgate, S. A., Fowler, T. K., Li, H., & Pino, J. 2014, ApJ, 789, 144
Colgate, S. A., & Li, H. 2004, CRPhy, 5, 431
Cronin, J. W. 1999, RvMP, 71, S165
de Gouveia Dal Pino, E. M., & Lazarian, A. 2005, A&A, 441, 845
de Gouveia Dal Pino, E. M., Alves Batista, R., Kowal, G., Medina-Torrejón, T., & Ramirez-Rodriguez, J. C. 2019, arXiv:1903.08982
Deng, W., Lin, Z., & Holod, I. 2012, NucFu, 52, 023005
Diehl, S., Li, H., Fryer, C. L., & Rafferty, D. 2008, ApJ, 687, 173
Fowler, T. K. 1981, in Fusion Part 1A, ed. E. Teller (New York: Academic) Chapter 5
Fowler, T. K., Colgate, S. A., & Li, H. 2009a, Lawrence Livermore National Laboratory Rep. LLNL-TR-14420
Fowler, T. K., & Gatto, R. 2007, PPCF, 49, 1673
Fowler, T. K., Jayakumar, R., & McLean, H. S. 2009b, JFuE, 28, 118
Fowler, T. K., & Li, H. 2016, JPlPh, 82, 595820513
Gan, Z., Li, H., Li, S., & Yuan, F. 2017, ApJ, 839, 14
Giannios, D., Uzdensky, D. A., & Begelman, M. C. 2009, MNRAS, 395, L29
Giovannini, G., Savolainen, T., Orienti, M., et al. 2018, NatAs, 2, 472
Goldston, R. J., & Rutherford, P. H. 1995, Introduction to Plasma Physics (Philadelpia: Institute of Physics Publishing)
Guan, X., Li, H., & Li, S. 2014, ApJ, 781, 48
Guo, F., Li, H., Daughton, W., & Liu, Y.-H. 2014, PhRvL, 113, 155005
Hawley, J. F., & Krolik, J. H. 2006, ApJ, 641, 103
Heinz, S. 2014, SSR, 183, 405
Hooper, E. B., Bulmer, R. H., Cohen, B. I., et al. 2012, PPCF, 54, 11300
Jackson, J. D. 1998, Classical Electrodynamic (3rd ed.; New York: Wiley)
Kadowaki, L. H. S., de Gouveia Dal Pino, E. M., Kowal, G., & Stone, J. M. 2018, ApJ, 864, 52
Kaufman, A. N. 1972, PhFl, 15, 1063

Komissarov, S. S., Barkov, M. V., Vlahakis, N., & Konigl, A. 2007, MNRAS, 380, 51
Kowal, G., de Gouveia Dal Pino, E. M., & Lazarian, A. 2011, ApJ, 735, 102
Krolik, J. H. 1999, Active Galactic Nuclei (Princeton: Princeton Univ. Press)
Kronberg, P. P., Lovelace, R. V. E., Lapenta, G., & Colgate, S. A. 2011, ApJL, 741, L15
Lazarian, A., & Vishniac, E. 1999, ApJ, 517, 700
Li, H., & Kusunose, M. 2000, ApJ, 536, 729
Li, H., Lapenta, G., Finn, J. M., Li, S., & Colgate, S. A. 2006, ApJ, 643, 92
Li, H., Lovelace, R. V. E., Finn, J. M., & Colgate, S. A. 2001, ApJ, 561, 915
Liu, W., Li, H., Yin, L., et al. 2011, PhPl, 18, 052105
Lovelace, R. V. E. 1976, Natur, 262, 649
Lovelace, R. V. E., & Kronberg, P. P. 2013, MNRAS, 430, 2828
Lovelace, R. V. E., Li, H., Koldoba, A. V., Ustyugova, G. V., & Romanova, M. M. 2002, ApJ, 572, 445
Lynden-Bell, D. 1996, MNRAS, 279, 389
Lynden-Bell, D. 2003, MNRAS, 341, 1360
Lynden-Bell, D. 2006, MNRAS, 369, 1167
Madejski, G. G., & Sikora, M. 2016, ARA&A, 54, 725
McClenaghan, J., Fowler, K., Li, H., & Lin, Z. 2014, New Orleans APS/DPP, TP8, 107
McDonald, D., & Thorne, K. S. 1982, MNRAS, 179, 433
McKinney, J. C., Tchekhovskoy, A., & Blandford, R. D. 2012, MNRAS, 423, 3083
McNamara, B. R., & Nulsen, P. E. J. 2007, AARA, 45, 117
Meier, D. L. 2012, Black Hole Astrophysics (New York: Springer Praxis)
Mizuno, Y., Hardee, P. E., & Nishikawa, K.-I. 2014, ApJ, 784, 167
Montgomery, D. C., & Tidman, D. A. 1964, Plasma Kinetic Theory (New York: McGraw-Hill)
Nakamura, M., Li, H., & Li, S. 2006, ApJ, 652, 1059
Nakamura, M., Li, H., & Li, S. 2007, ApJ, 656, 721
Narayan, R., McKinney, J. C., & Farmer, A. J. 2007, MNRAS, 375, 548
Norman, M. L., Winkler, K.-H. A., Smarr, L., & Smith, M. D. 1982, A&A, 113, 285
Owen, F. N., Hardee, P. E., & Cornwell, T. J. 1989, ApJ, 340, 698
Pariev, V. I., & Colgate, S. A. 2007, ApJ, 658, 114
Pariev, V. I., Colgate, S. A., & Finn, J. M. 2007, ApJ, 658, 129
Pierre Auger Collaboration 2007, Sci, 318, 938
Pierre Auger Collaboration 2014, ApJ, 794, 172
Pierre Auger Collaboration 2017, Sci, 357, 1266
Post, R. F. 1981, in Fusion Part 1A, ed. E. Teller (New York: Academic) Chapter 6
Post, R. F., & Rosenbluth, M. N. 1966, PhFl, 9, 730
Robinson, D. R. 1978, NucFu, 18, 939
Rusbridge, M. S., Gee, S. J., Browning, P. K., et al. 1997, PPCF, 39, 683
Singh, C. B., Mizuno, Y., & de Gouveia Dal Pino, E. M. 2016, ApJ, 824, 48
Sironi, L., & Spitkovsky, A. 2014, ApJL, 783, L21
Smith, G. R., & Cohen, B. I. 1983, PhFl, 26, 238
Spruit, H. C., Foglizzo, T., & Stehle, R. 1997, MNRAS, 288, 333
Tchekhovskoy, A., & Bromberg, O. 2016, MNRAS, 461, L46
Tchekhovskoy, A., McKinney, J. C., & Narayan, R. 2008, MNRAS, 388, 151
Ustyugova, G. V., Koldoba, A. V., Romanova, M. M., Chechetkin, V. M., & Lovelace, R. V. E. 1999, ApJ, 516, 221
Werner, G. R., Uzdensky, D. A., Cerutti, B., Nalewajko, K., & Begelman, M. C. 2016, ApJL, 816, L8
Zhai, A. X., Li, H., Bellan, P. M., & Li, S. 2014, ApJ, 791, 40
Zhang, H., Li, H., Guo, F., & Taylor, G. 2017, ApJ, 835, 125